
Functional Renormalization Group Applied to a Multimode Quantum Point Contact

Katharina Eissing



Master's Thesis
Chair of Theoretical Solid State Physics
Faculty of Physics
Ludwig-Maximilians-University Munich
Supervisor: Prof. Dr. Jan von Delft

April 2, 2013

Funktionale Renormierungsgruppe angewendet auf einen mehrmodigen Quantenpunktkontakt

Katharina Eissing



Masterarbeit
Lehrstuhl für Theoretische Festkörperphysik
Fakultät für Physik
Ludwig-Maximilians-Universität München
Betreuer: Prof. Dr. Jan von Delft

2. April 2013

Contents

1. Introduction	1
2. Functional Renormalization Group (fRG)	3
2.1. Introduction	3
2.2. Vertex functions and Green's functions	4
2.3. Diagrammatical derivation of fRG flow equations	6
2.4. Truncation	10
2.5. Static fRG	10
2.6. Λ -dependence	10
2.7. Final structure of fRG 2	11
2.8. Symmetries	14
3. Quantum Point Contacts (QPC)	17
3.1. One-dimensional transport through a QPC	17
3.2. Conductance quantization	18
3.3. Conductance anomaly	19
3.4. 0.7 anomaly as an interaction effect	21
4. fRG applied to a QPC with n subbands	27
4.1. Model	27
4.2. fRG equations	29
4.3. Observables	33
4.3.1. Conductance	33
4.3.2. Local density	33
4.3.3. Local magnetization	34
4.3.4. Spin susceptibility	34
4.3.5. Low-energy scale B^*	34
5. Results	35
5.1. Effect of one higher order term on the conductance of a one-band model	35
5.2. QPC modelled with two subbands	38
5.3. QPC modelled with four subbands	50
5.4. Effect of one half-filled subband on the conductance	58
6. Conclusion and Outlook	61
A. Transport through coupled quantum wires	63
A.1. Models	63
A.1.1. Model I	63
A.1.2. Model II	64
A.2. Results	65

List of Figures

3.1.	Picture of experimental setup of a quantum point contact	17
3.2.	Experimental measurement of the linear differential conductance $G = \frac{dI}{dV}$ as a function of gate voltage	19
3.3.	Evolution of the conductance with increasing temperature and increasing magnetic field.	20
3.4.	Dispersion relation and density of states of a tight-binding model and the density of states within the band shaped by a barrier potential.	21
3.5.	Barrier potential and corresponding peak of the spectral function in the center of the constriction for three different heights of the barrier.	22
3.6.	Local density plotted as a function of the site number	23
3.7.	Local density and conductance as a function of gate voltage for the central site.	24
4.1.	Illustration of the used model for $n = 2$	27
5.1.	Comparison of vertex functions at the central site and conductance plotted against gate voltage for one band	36
5.2.	Comparison of the conductance as a function of gate voltage for several values of a magnetic field B for the purely second order model and the one with the extra D structure	36
5.3.	Low-energy scale B^* logarithmic plotted as a function of gate voltage computed with and without the extra $D_{0,0}^{\uparrow,\downarrow}$ structure	37
5.4.	Comparison of conductance and vertex functions on the central site for two different choices of the interaction plotted as a function of gate voltage	38
5.5.	Conductance as a function of gate voltage for two different sublevel spacings ΔE	39
5.6.	Low-energy scale B^* plotted logarithmically as a function of gate voltage for the first and second subband in the cases of equal and different interactions	40
5.7.	Local density as a function of gate voltage (5.7a) and as a function of the number of site j for several values of B (5.7b).	41
5.8.	The local magnetization as a function of the site number j for several values of the magnetic field B and equal interactions	42
5.9.	The local magnetization as a function of the site number j for several values of the magnetic field B and different interactions	45
5.10.	The local susceptibility as a function of the site number j for several values of the magnetic field B and equal interactions	46
5.11.	The local susceptibility as a function of the site number j for several values of the magnetic field B and different interactions	47
5.12.	Total susceptibility for different and equal interactions as a function of gate voltage.	48

5.13. Conductance plotted as a function of gate voltage for several values of the interaction U_1	49
5.14. Conductance plotted as a function of gate voltage for a four-band model with different interactions	50
5.15. Low-energy scale B^* plotted logarithmically as a function of gate voltage for the four subbands.	51
5.16. Comparison of the conductance steps and the derivative of the conductance in a four-band model with different interactions.	51
5.17. Conductance and vertex function at the central site plotted as a function of gate voltage for a four-band model in the case of different interactions	52
5.18. Conductance and total susceptibility as a function of gate voltage for several value of interaction U_1	53
5.19. Local density in case of different interactions	53
5.20. Conductance plotted as a function of gate voltage for a four-band model with equal interactions	54
5.21. Derivative of the conductance and low-energy scale B^* in case of equal interactions	55
5.22. Conductance and vertex function at the central site plotted as a function of gate voltage for a four-band model in the case of equal interactions	56
5.23. Local density in case of equal interactions	56
5.24. Conductance plotted as a function of gate voltage for a four-band model for several values of the interaction in the case of equal interactions	57
5.25. Conductance of the second band as a function of gate voltage with a half-filled first subband.	58
5.26. Conductance and vertex function at the central site of the second subband as a function of gate voltage with a half-filled first subband.	59
5.27. Local density of the first and second subband in case of an initial half-filled first subband for equal and different interactions.	60
5.28. Comparison of the conductance of the second band under the influence of a half-filled subband for equal and different interactions	60
A.1. Model I with two leads	63
A.2. Model II without finite ends	64
A.3. Conductance as a function of number of sites and interchain hopping τ_{12} for model I and II	65
A.4. Comparison of numerical computed conductance with the transmission formula of model I	66
A.5. Conductance plotted as a function of temperature for both models.	68
A.6. Comparison of the interacting with the noninteracting system in model I . . .	68

1. Introduction

Developing devices on a nanoscale is one of the main goals of current research in nanophysics. A key prerequisite for designing properly functioning nanodevices is a profound understanding of the physics of transport on this scale. This is subject of the striking field of quantum transport. One important example of such nanodevices is the quantum point contact (QPC). It is a short quantum wire that allows to observe quasi-one-dimensional transport. Its first application has been reported by van Wees et al. [1] and simultaneously by Wharam et al. [2] in 1988, who observed quantized conductance within the QPC. Measuring conductance as a function of gate voltage one observes that with decreasing gate voltage the conductance reduces in equal steps. Each plateau is a multiple of the so-called conductance quantum $G_Q = 2e^2/h$. This observation can be explained in a single-particle picture as the decreasing number of contributing transport channels.

In 1996 Thomas et al. [3] adressed a feature, that became famous as the '0.7 anomaly'. It concerns the anomalous behaviour of the first step of the quantized conductance, which exhibits a shoulder that enhances with increasing magnetic field and temperature. This has led to a lively debate about the origin of this anomaly. While all possible explanations agree that the electron-electron interactions causes this phenomenon, they differ widely regarding the detailed mechanisms by which this happens.

Bauer et al. [4] approach this problem within a fRG scheme and identify a smeared van Hove singularity as the origin of the 0.7 anomaly. They argue that the shoulder is a consequence of an enhanced Hartree effect when the van Hove ridge passes the chemical potential. This effect is even more pronounced in a parallel magnetic field, which increases the effective Landé factor.

The present thesis is motivated by their work and aims to model a QPC with n subbands to observe conductance for more than one transport channel through it. To this end, Bauer's model is extended up to n chains, representing the n subbands. Interactions on one chain as well as between the chains are modeled using on-site interactions, and interband transitions are neglected. Calculations are performed using the functional Renormalization Group, which is a powerful method to treat interacting many-body systems ([5], [6], [7]). The main issue of interest here is the open question why the 0.7 anomaly is typically significantly stronger for the first than for higher conductance steps. First results point out that the first conductance step behaves differently compared to the higher steps.

The thesis is structured as follows: In the subsequent chapter an introduction to the method of functional Renormalization Group is presented, where a diagrammatical approach is used to derive the fRG equations. The third chapter introduces the setup of a QPC, describes the conductance quantization and the observations linked to the 0.7 anomaly. Further, the key points of the explanation of Bauer et al. are presented, which is background to interpret the results of this work. In chapter 4 a detailed explanation of the model and a derivation of

the concrete fRG equations within this model, are given and all computed observables will be defined. In the fifth chapter the numerical results are presented. Firstly, the comparison of a one-band model with the utilized n -band model offers the possibility to investigate the effect of one higher order term in the fRG equations on the conductance of the one-band model. Secondly, models with two and with four subbands are considered for two different choices of interaction in this system. Here several observables such as conductance and local density are computed. Moreover, the conductance of a band that interacts with a half-filled subband is studied. In the last chapter, we conclude and give an outlook on possible future research within this topic.

2. Functional Renormalization Group (fRG)

In this chapter the functional Renormalization Group (fRG) is explained. Since there are already a lot of very good derivations of the fRG differential equations (e.g. [8], [9], [10]) via the strict functional integral formalism, a diagrammatical approach is used as it has been done by Jakobs ([11], [12]). This chapter starts with an introduction to the keynote of fRG, then some diagrammatic vocabulary will be set up to use it for the subsequent derivation. This is followed by some comments on the used truncation, the flow parameter dependence and on the approximation of static fRG. Lastly, the final fRG equations are derived and symmetries are explained.

2.1. Introduction

Functional Renormalization Group is a 'renormalization group enhanced perturbation theory' [10] for the treatment of interacting many-body systems. It is based on the renormalization group scheme (RG) developed by K.G. Wilson and uses the functional integral formulation of many-body physics. fRG is a very powerful method, which yields results which can be superior to perturbation theory results ([5], [6],[7]).

The fundamental idea of fRG is to introduce an infrared cutoff Λ which serves as flow parameter, take the derivative of the vertex functions with respect to this flow parameter and subsequently study the behaviour in the limit $\Lambda \rightarrow 0$, i.e. in the limit of the original system [10]. This way, it can be used for low dimensional systems, which show infrared divergencies.

Thus, fRG is based on a hierarchy of differential equations of n-particle vertex functions γ_n with respect to the flow parameter Λ

$$\frac{d}{d\Lambda}\gamma_n = \mathcal{F}(\gamma_1, \gamma_2, \dots, \gamma_{n+1}, \Lambda) \quad (2.1)$$

where as we will see later the derivative of the nth vertex function depends on all other up to the (n+1)th vertex function and on the flow parameter. The flow parameter is introduced into the Green's function

$$G^0 \rightarrow G^{0,\Lambda} \quad (2.2)$$

such that

$$G^{0,\Lambda_{initial}} = 0 \quad G^{0,\Lambda_{final}} = G^0 \quad (2.3)$$

holds. Integration from $\Lambda_{initial}$ to Λ_{final} can be regarded as an integration from bare interaction to the full, renormalized interaction. This point becomes clear, when the vertex functions are defined diagrammatically in the subsequent section.

The main goal is to solve these differential equations to obtain solutions for the vertex functions. In particular, one is interested in the one-particle vertex function Σ to facilitate calculation of the full, renormalized Green's function \mathcal{G} via the well-known Dyson equation

$$\mathcal{G} = \frac{1}{(G^0)^{-1} - \Sigma}. \quad (2.4)$$

The full, renormalized Green's function \mathcal{G} in turn can be used to compute several observables.

In general this infinite hierarchy of differential equation cannot be solved exactly. Thus, different truncation and approximation schemes have been developed. Later in this chapter, the commonly used static fRG and the truncation schemes are explained.

2.2. Vertex functions and Green's functions

As a first step some graphic representations is set up, i.e. some graphic 'vocabulary' which is needed to derive the fRG equations diagrammatically. We will work in a simple frame, where we assume point-like and frequency independent two particle interaction. Therefore the bare interaction between two incoming and two outgoing particles is denoted with U and graphically represented by a black dot.

$$U = \bullet \quad (2.5)$$

Next, there is the non-interacting, single-particle Green's function, also denoted as free propagator. It has been set to depend on the flow parameter Λ and is graphically represented as a bare line

$$G^{0,\Lambda} = \text{—————} \quad (2.6)$$

The so-called full Green's function is the sum of all possible ways to connect two points with the free propagator via any number of interaction events. It is represented as

$$\mathcal{G}^\Lambda = \text{=====} \quad (2.7)$$

A first step to use the diagrammatic language is to clarify what is meant by a full Green's function and derive the Dyson equation eq.(2.4) in this representation:

$$\begin{aligned}
 \text{Full Propagator} &= \text{---} + \text{---} \circlearrowleft \text{---} + \text{---} \circlearrowleft \circlearrowleft \text{---} + \text{---} \circlearrowleft \circlearrowleft \circlearrowleft \text{---} + \text{---} \circlearrowleft \circlearrowright \text{---} \\
 &+ \text{---} \circlearrowright \circlearrowleft \text{---} + \text{---} \circlearrowleft \circlearrowleft \circlearrowleft \text{---} + \dots \\
 &= \text{---} + \text{---} \circlearrowleft \left(\text{---} + \text{---} \circlearrowleft + \text{---} \circlearrowleft \circlearrowleft + \dots \right) \\
 &+ \text{---} \circlearrowleft \left(\text{---} + \text{---} \circlearrowleft + \text{---} \circlearrowleft \circlearrowleft + \dots \right) \\
 &+ \dots \\
 &= \text{---} + \text{---} \circledast \text{---} \quad (2.8)
 \end{aligned}$$

The full propagator is the sum of all connected diagrams with one incoming and one outgoing particle as sketched in the first line of eq.(2.8). This sum consists of two types of diagrams: There are diagrams which can be separated into two parts by just cutting one line, called one-particle reducible diagrams. And there are those diagrams which cannot be separated by cutting one line, which are called one-particle irreducible (1PI) diagrams.

Further one can see that the reducible diagrams can be built of the irreducible ones. We can now reorder this sum of diagrams such that the 1PI diagrams are factored out and a reducible diagram is represented by multiplying two diagrams. This way we multiply the sum of all one-particle irreducible diagrams with an infinite sum of all connected diagrams containing reducible and irreducible diagrams, i.e. the full propagator. The sum of all connected, one-particle irreducible diagrams with two amputated legs is called self-energy Σ and is graphically denoted with a circle. Finally, one ends up with the diagrammatic illustration of the well known Dyson equation (2.4).

The first few diagrams of the infinite sum of diagrams of the self-energy are:

$$\Sigma = \text{---} \circledast \text{---} = \text{---} \circlearrowleft \text{---} + \text{---} \circlearrowleft \circlearrowleft \text{---} + \text{---} \circlearrowleft \circlearrowright \text{---} + \text{---} \circlearrowleft \circlearrowleft \circlearrowleft \text{---} + \text{---} \circlearrowleft \circlearrowleft \circlearrowleft \circlearrowleft \text{---} + \dots \quad (2.9)$$

Analogously to the self-energy, one can define any n-particle vertex function γ_n as the sum of all connected, one-particle irreducible diagrams with 2n amputated legs. The first contributing diagrams of the two-particle vertex function γ_2 are depicted below, where lowest

order diagram is the bare interaction. This vertex function γ_2 is illustrated by a rectangle.

$$\gamma_2 = \text{rectangle} = \bullet + \text{loop} + \text{two-loops} + \text{triangle} + \text{two-loops-triangle} + \dots \quad (2.10)$$

As a last example, the first diagram of the three-particle vertex function is depicted below. This vertex function is represented by a hexagon:

$$\gamma_3 = \text{hexagon} = \text{triangle} + \dots \quad (2.11)$$

Finally, a derivative of the free propagator with respect to the flow parameter Λ is represented with a crossed out line

$$\partial_\Lambda G^{0,\Lambda} = \text{crossed-out line} \quad (2.12)$$

Now, we have set up the diagrammatical representation of all objects we need and we can start with the derivation of the flow equations.

2.3. Diagrammatical derivation of fRG flow equations

As mentioned in the introduction the flow parameter Λ is introduced into the Green's function such that $G^{0,\Lambda_{initial}}$ is zero and $G^{0,\Lambda_{final}}$ is the ordinary propagator. If we consider the initial situation and set all propagators to zero in all vertex functions, the only remaining diagram is the bare interaction. For $\Lambda = \Lambda_{initial}$, all γ_n ($n \neq 2$) are zero, while γ_2 equals the bare interaction. Thus, integrating from $\Lambda_{initial}$ to Λ_{final} is equivalent to

$$\bullet \rightarrow \text{rectangle} \quad (2.13)$$

i.e. it is integrated from bare interaction up to the full interaction.

As a first step to set up the fRG equations we take the derivative of the vertex functions with respect to the flow parameter. There is a Λ - dependence in each propagator, but the bare two-particle interaction does not depend on it. Graphically that leads to one crossed out line in each diagram and of course one needs to use the chain rule and take the derivative of each line, i.e. of each free Green's function in the diagram. For the self-energy this is depicted below:

$$\begin{aligned}
\frac{d}{d\Lambda}\Sigma = \frac{d}{d\Lambda} \text{ (shaded circle) } = & \text{ (loop) } + \text{ (bubble) } + \text{ (bubble) } + \text{ (bubble) } \\
& + \text{ (bubble) } + \text{ (bubble) } + \text{ (bubble) } \\
& + \text{ (bubble) } + \text{ (bubble) } + \dots \\
& + \text{ (triangle) } + \text{ (triangle) } + \text{ (triangle) } + \dots \quad (2.14)
\end{aligned}$$

The derived diagrams are reordered in the next step such that they can be rewritten in terms of the vertex functions. This needs to be done in the following manner: Imagine the diagram without the crossed out line and find all 1PI subdiagrams. Each subdiagram is marked with the dotted sign of the according vertex function to which it belongs.

$$\begin{aligned}
\frac{d}{d\Lambda}\Sigma = \frac{d}{d\Lambda} \text{ (shaded circle) } = & \text{ (loop) } + \text{ (bubble) } + \text{ (bubble) } + \text{ (bubble) } + \dots \\
& + \text{ (bubble) } + \text{ (bubble) } + \text{ (bubble) } + \dots \\
& + \text{ (triangle) } + \text{ (triangle) } + \text{ (triangle) } + \dots \quad (2.15)
\end{aligned}$$

For example, the pure interaction belongs to the two-particle vertex function and therefore it is marked with a rectangle in the lower part of the first diagram. Equally the marked bubble in the second diagram belongs to γ_2 , because it is the second diagram in eq. (2.10). In the third diagram one of the lower legs is crossed out. This divides the diagram into two 1PI subdiagrams. Here, the closed loop with the interaction belongs to the self-energy, while the lower interaction belongs again to γ_2 . This way one can proceed with all diagrams.

In the next step, all marked diagrams that show the same structure are grouped together. In eq. (2.15) most of the diagrams belong to the same structure. These diagrams include a part that belongs to γ_2 and a crossed out propagator. The third diagram shows a slightly different structure of a part that belongs to γ_2 and a subdiagram that belongs to the self-energy, connected by a full propagator and a crossed out propagator. Two of the diagrams in the last line are constructed of a subdiagram that belongs to γ_2 , which is connected by

one crossed out propagator and two free propagators to two subdiagrams that belong to the self-energy. Hence, all diagrams are constructed of a γ_2 with a closed loop of one crossed out propagator, any number of self-energies and a corresponding number of free propagators. Diagrams with the same structure then sum up to the following equation:

$$\frac{d}{d\Lambda}\Sigma = \frac{d}{d\Lambda} \text{ (shaded circle) } = \text{ (shaded circle with top line crossed) } + \text{ (shaded circle with top and bottom lines crossed) } + \text{ (shaded circle with top, bottom, and left lines crossed) } + \dots \quad (2.16)$$

To add up all these diagrams a so called the single scale propagator S is defined. The single scale propagator is the sum of all diagrams which contribute to the full Green's function where the derivative is taken of one free propagator. This free propagator needs to be such a line that by cutting it, the diagram is divided into two parts. In diagrams, this can be written:

$$\begin{aligned} & \text{---/---} + \text{---/ (shaded circle) ---} + \text{--- (shaded circle) /---} + \text{--- (shaded circle) /--- (shaded circle) ---} + \dots \\ &= \left(\text{--- (shaded circle) ---} + 1 \right) \text{---/---} \left(1 + \text{--- (shaded circle) ---} \right) \\ &= \left(\text{--- (shaded circle) ---} + \text{---} \right) \left[\text{---} \right]^{-1} \text{---/---} \left[\text{---} \right]^{-1} \left(\text{---} + \text{--- (shaded circle) ---} \right) \\ &= \text{---/---} \\ &= S^\Lambda \end{aligned} \quad (2.17)$$

where in the third line a $[G^{0,\Lambda}]^{-1}$ is factored out. The single scale propagator is represented by a double, crossed out line and defined as:

$$S^\Lambda = \mathcal{G}^\Lambda [G^{0,\Lambda}]^{-1} \partial_\Lambda G^{0,\Lambda} [G^{0,\Lambda}]^{-1} \mathcal{G}^\Lambda = \mathcal{G}^\Lambda \partial_\Lambda [G^{0,\Lambda}]^{-1} \mathcal{G}^\Lambda \quad (2.18)$$

Using this definition of the single scale propagator it leads to :

$$\frac{d}{d\Lambda}\Sigma = \frac{d}{d\Lambda} \text{ (shaded circle) } = \text{ (shaded circle with top line crossed) } \quad (2.19)$$

Hence, we end up with one structure and equation (2.19) is the diagrammatical representation of the first equation of the fRG hierarchy. As predicted the derivative of Σ depends on the two-particle vertex function.

The same procedure can be applied to the two-particle vertex function. Again the derivative is taken obeying chain rule

$$\frac{d}{d\Lambda} \gamma_2 = \frac{d}{d\Lambda} \text{[diagram]} = \text{[diagram 1]} + \text{[diagram 2]} + \dots$$

$$+ \text{[diagram 3]} + \text{[diagram 4]} + \dots$$

$$+ \text{[diagram 5]} + \text{[diagram 6]} + \text{[diagram 7]} \quad \text{\#(2.20)}$$

Subsequently the 1PI subdiagrams are marked according to their belonging

$$\frac{d}{d\Lambda} \gamma_2 = \frac{d}{d\Lambda} \text{[diagram]} = \text{[diagram 1]} + \text{[diagram 2]}$$

$$+ \text{[diagram 3]} + \text{[diagram 4]} + \dots$$

$$+ \text{[diagram 5]} + \text{[diagram 6]} + \text{[diagram 7]} + \dots \quad (2.21)$$

Ordering and adding up the diagrams with respect to their structure, yields the following representation.

$$\frac{d}{d\Lambda} \gamma_2 = \frac{d}{d\Lambda} \text{[diagram]} = \text{[diagram 1]} + \text{[diagram 2]} + \text{[diagram 3]} + \dots$$

$$+ \text{[diagram 4]} + \dots$$

$$= \text{[diagram 5]} + \text{[diagram 6]} \quad (2.22)$$

In the last step the definition of the single scale propagator (eq.(2.17)) has been used again. Equation (2.22) describes the second differential equation of the fRG hierarchy. Here we have two types of structure, one that depends on the two-particle vertex function and one that depends on the three-particle vertex function. We could proceed for all vertex function, and we will always see that the derivative of the n-particle vertex function depends on all vertex functions up to the (n+1)th vertex function. Since this poses an infinite hierarchy, truncation is required at some point.

2.4. Truncation

In general, one can truncate at any point. Later truncation yields more precise results, but solving the equations becomes less feasible. A truncation after the m th vertex function, with

$$\frac{d}{d\Lambda}\gamma_{m+1} = 0 \quad (2.23)$$

is called fRG m . The most commonly used truncations are fRG 1 and fRG 2.

fRG 1 includes only the first equation (eq.(2.19)) and the vertex flow is neglected i.e. the full vertex function γ_2 in this equation is substituted with the bare interaction U . This yields qualitatively good results and can give a good impression of the physics of a system.

Truncation after the two-particle vertex function yields to quantitatively better results. To set

$$\frac{d}{d\Lambda}\gamma_{m+1} = 0 \quad \text{with} \quad m \geq 2 \quad (2.24)$$

can be justified as follows:

As in perturbation theory the bare interaction needs to be small to ensure convergency. While the lowest order diagrams in Σ and γ_2 are generated in first order in the interaction, all diagrams of the three-particle vertex function are generated at least in third order of the interaction. It is thus reasonable to neglect those higher order diagrams.

For fRG 2 the derivative of γ_3 is set to zero, i.e. the second structure of equation (2.22) is canceled out.

2.5. Static fRG

In general, all Green's functions and vertex functions depend on frequency. Consequently, within the Matsubara formalism an infinite sum over all possible frequencies needs to be evaluated. Static fRG neglects the entire frequency dependence of the vertex function and thus the frequency dependence of the external vertices. Therefore internal frequencies need to add up to zero to ensure energy conservation.

Results of static fRG can only be trusted in the limit of $\omega \rightarrow 0$, i.e. for $T = 0$. In this work, static fRG is used and therefore all results are only valid for zero temperature.

2.6. Λ -dependence

In the introduction it has already been mentioned that an infrared cutoff is needed which works as a flow parameter Λ . This flow parameter has been introduced into the Green's function, but no precise dependence has been determined. Since possible divergencies in low dimensional systems usually show up for energies around the zero-point of the energy scale, a convenient choice of Λ dependence for $T = 0$ is

$$G^{0,\Lambda} = \theta(|\omega| - \Lambda)G^0. \quad (2.25)$$

with θ as the Heaviside-function. For a detailed justification read [13]. Since we work with static fRG, we stick to the case of $T = 0$ for the whole thesis and can use this cutoff. With $\Lambda_{initial} = \infty$ and $\Lambda_{final} = 0$ this dependence then leads to $G^{0,\Lambda_{initial}} = 0$ and $G^{0,\Lambda_{final}} = G^0$ as demanded in the beginning.

2.7. Final structure of fRG 2

In our diagrammatical illustration of the structure of the fRG equations, we did not use any arrows, i.e. no directions have been considered until now. This is fine as long as one keeps in mind that each structure includes several topological different diagrams. To set up the final equations we also need to take into account directions of the participating particles and add some further Feynman rules to the diagrammatical representations:

- Draw all topological different diagrams. Topological different diagrams are those which cannot be deformed into each other including all arrows and external indices.
- Multiply with $(-1)^F$ with F as the number of closed fermion loops.
- Multiply with (-1) for each interchange of external legs.
- Sum over the Matsubara frequencies \sum_{w_n} .
- If two fermion lines form a closed loop their frequencies are equal and with opposite signs, if they propagate in the same direction (static fRG).
- Sum over all internal indices $\sum_{q,q',s,s'}$.

For the first differential equation, there is only one diagram because any other can be deformed into this one. Blue and red arrows indicate the external indices of the incoming and outgoing amputated legs, respectively. The final equations we set up for γ_1 instead of Σ . It is defined as $\gamma_1 = -\Sigma$, hence there is an extra minus which leads to:

$$\frac{d}{d\Lambda}\gamma_1(k'_1, k_1) = -\frac{d}{d\Lambda}\Sigma(k'_1, k_1) = \frac{d}{d\Lambda} \left(\text{diagram with shaded circle} \right) = \text{diagram with shaded circle with loop} \quad (2.26)$$

For fRG 2 the second structure in eq. (2.22) is canceled out. Thus, we are left with only one structure, which includes five topological different diagrams:

$$\begin{aligned}
\frac{d}{d\Lambda} \gamma_2(k'_1, k'_2, k_1, k_2) &= \frac{d}{d\Lambda} \left[\text{Diagram 1} \right] = - \left[\text{Diagram 2} \right] \\
&- \left[\text{Diagram 3} \right] - \left[\text{Diagram 4} \right] \\
&+ \left[\text{Diagram 5} \right] + \left[\text{Diagram 6} \right] \tag{2.27}
\end{aligned}$$

This is the final version of the fRG equation, with truncation after the two-particle vertex function. So far, no further approximations have been made. The signs are already evaluated here to give a better overview of the structure of the equations.

Now, static fRG and the respective cutoff for zero temperature get involved. If the cutoff (2.25) is introduced into the Green's function, the single-scale propagator can be rewritten as follows:

$$\begin{aligned}
S^\Lambda &= \mathcal{G}^\Lambda \partial_\Lambda [G^{0,\Lambda}]^{-1} \mathcal{G}^\Lambda \\
&= \frac{1}{1 + \theta G^0 \gamma_1^\Lambda} \theta G^0 [G^0]^{-1} \frac{1}{\theta^2} \delta \frac{1}{1 + \theta G^0 \gamma_1^\Lambda} \theta G^0 \\
&= \frac{\delta}{(1 + \theta G^0 \gamma_1^\Lambda)^2} G^0 \\
&= \delta \partial_\theta \left[\frac{1}{1 + \theta G^0 \gamma_1^\Lambda} \theta G^0 \right] \\
&= \delta(|\omega| - \Lambda) \partial_\theta \mathcal{G}^\Lambda \tag{2.28}
\end{aligned}$$

where a short notation has been used with $\theta = \theta(|\omega| - \Lambda)$ and respectively $\delta = \delta(|\omega| - \Lambda)$.

Due to static fRG only the propagator is frequency dependent and therefore, the sum over the Matsubara frequencies can be evaluated separately. Further, in the limit of $T = 0$ the

Matsubara sum becomes an integral. With the rewritten single scale propagator (2.28)

$$\begin{aligned}
& \frac{1}{2\pi} \int d\omega S_{q,q'}^\Lambda(i\omega) \\
&= \frac{1}{2\pi} \int d\omega \delta(|\omega| - \Lambda) \partial_\theta \mathcal{G}^\Lambda \\
&\stackrel{(*)}{=} \frac{1}{2\pi} \int d\omega \delta(|\omega| - \Lambda) \int_0^1 dt \partial_t \mathcal{G}_{q,q'}^\Lambda(i\omega)|_{\theta=t} \\
&= \sum_{\omega=\pm\Lambda} \tilde{\mathcal{G}}_{q',q}^\Lambda(i\omega). \tag{2.29}
\end{aligned}$$

In the last step a new propagator is defined, where now only the self-energy depends on Λ :

$$\tilde{\mathcal{G}}^\Lambda = \frac{1}{[G^0]^{-1} - \Sigma_1^\Lambda}. \tag{2.30}$$

Also the diagrammatic illustration is redefined:

$$\tilde{\mathcal{G}}^\Lambda = \longrightarrow \tag{2.31}$$

The (*) in (2.29) and (2.33) indicates the use of the so-called Morris' Lemma [14], which states that

$$\delta_\epsilon f(\theta_\epsilon) \rightarrow \delta \int_0^1 f(t) dt \tag{2.32}$$

for a product of δ - and θ -function, which are defined as the limits of smooth functions $\delta = \lim_{\epsilon \rightarrow 0} \delta_\epsilon$ and $\theta = \lim_{\epsilon \rightarrow 0} \theta_\epsilon$ and where f can be any continuous function.

Analogously, this can be done for the integral over the single scale propagator and the Green's function as it is needed for the diagrams of the second equation.

$$\begin{aligned}
& \frac{1}{2\pi} \int d\omega S_{q,q'}^\Lambda(i\omega) \tilde{\mathcal{G}}_{s',s}^\Lambda(\pm i\omega) \\
&\stackrel{(*)}{=} \frac{1}{2\pi} \int d\omega \delta(|\omega| - \Lambda) \int_0^1 dt [\partial_t \mathcal{G}_{q,q'}^\Lambda(i\omega)]_{\theta=t} [\tilde{\mathcal{G}}_{s',s}^\Lambda(\pm i\omega)]_{\theta=t} \\
&= \frac{1}{2\pi} \int d\omega \delta(|\omega| - \Lambda) \int_0^1 dt \frac{1}{2} \partial_t [\mathcal{G}_{q,q'}^\Lambda(i\omega)]_{\theta=t} [\tilde{\mathcal{G}}_{s',s}^\Lambda(\pm i\omega)]_{\theta=t} \\
&= \frac{1}{4\pi} \int d\omega \delta(|\omega| - \Lambda) \tilde{\mathcal{G}}_{q',q}^\Lambda(i\omega) \tilde{\mathcal{G}}_{s',s}^\Lambda(\pm i\omega) \\
&= \frac{1}{4\pi} \sum_{\omega=\pm\Lambda} \tilde{\mathcal{G}}_{q',q}^\Lambda(i\omega) \tilde{\mathcal{G}}_{s',s}^\Lambda(\pm i\omega) \tag{2.33}
\end{aligned}$$

Due to the introduction of the redefined propagator, the second and the third, as well as the fourth and the fifth diagram become equal in eq. (2.27). It leads to an extra factor of 2 for these diagrams.

If Feynman rules are applied to evaluate the diagrams, with eq. (2.29) and (2.33), it leads to the final fRG 2 equations:

$$\frac{d}{d\Lambda} \gamma_1^\Lambda(k', k) = \frac{1}{2\pi} \sum_{\omega=\pm\Lambda} \sum_{q, q'} \tilde{\mathcal{G}}_{q, q'}^\Lambda(i\omega) \gamma_2^\Lambda(k', q'; k, q), \quad (2.34)$$

$$\begin{aligned} \frac{d}{d\Lambda} \gamma_2^\Lambda(k'_1, k'_2; k_1, k_2) = & \\ \frac{1}{2\pi} \sum_{\omega=\pm\Lambda} \sum_{q, q', s, s'} & \left[-\frac{1}{2} \tilde{\mathcal{G}}_{q, q'}^\Lambda(i\omega) \gamma_2^\Lambda(q', s'; k_1, k_2) \tilde{\mathcal{G}}_{s, s'}^\Lambda(-i\omega) \gamma_2^\Lambda(k'_1, k'_2; s, q) \right. \\ & - \tilde{\mathcal{G}}_{q, q'}^\Lambda(i\omega) \gamma_2^\Lambda(k'_1, q'; k_1, s) \tilde{\mathcal{G}}_{s, s'}^\Lambda(i\omega) \gamma_2^\Lambda(k'_2, s'; k_2, q) \\ & \left. + \tilde{\mathcal{G}}_{q, q'}^\Lambda(i\omega) \gamma_2^\Lambda(k'_2, q'; k_1, s) \tilde{\mathcal{G}}_{s, s'}^\Lambda(i\omega) \gamma_2^\Lambda(k'_1, s'; k_2, q) \right]. \end{aligned} \quad (2.35)$$

And in their diagrammatically representation:

$$\frac{d}{d\Lambda} \gamma_1(k'_1, k_1) = \frac{d}{d\Lambda} \left(\text{diagram: red arrow } k'_1 \text{ to a shaded circle, blue arrow } k_1 \text{ from it} \right) = \text{diagram: red arrow } k'_1 \text{ to a shaded rectangle, blue arrow } k_1 \text{ from it} \quad (2.36)$$

$$\begin{aligned} \frac{d}{d\Lambda} \gamma_2(k'_1, k'_2, k_1, k_2) = & \frac{d}{d\Lambda} \left(\text{diagram: shaded square with four arrows } k'_1, k_1, k'_2, k_2 \right) \\ = & -\frac{1}{2} \left(\text{diagram: shaded rectangle with two arrows } k'_1, k'_2 \text{ and two } k_1, k_2 \right) \\ & - \left(\text{diagram: shaded rectangle with two arrows } k'_1, k_1 \text{ and two } k'_2, k_2 \right) \\ & + \left(\text{diagram: shaded rectangle with two arrows } k'_2, k_1 \text{ and two } k'_1, k_2 \right) \end{aligned} \quad (2.37)$$

The final differential equation of the two particle vertex function consists of three different structures. Each represents one of the three channels of two-particle interaction. While the first diagram represents the particle-particle interaction (P-channel), the second and third diagram represent particle-hole interactions. The two contributions only differ in an interchange of legs and represent according to their structure the direct interaction (D-channel) and exchange interaction (X-channel), respectively.

2.8. Symmetries

The symmetries of the two particle vertex function can be derived if one takes into account the Feynman rule for exchanging external legs. It is then easy to see that γ_2 is antisymmetric

under the exchange of the incoming particles with each other and analogously under the exchange of the outgoing particles. Further, in the special case of static fRG and time reversal symmetry the vertex function becomes symmetric under the exchange of the incoming with the outgoing particles.

$$\begin{aligned}\gamma_2(k'_1, k'_2, k_1, k_2) &= -\gamma_2(k'_2, k'_1, k_1, k_2) \\ &= -\gamma_2(k'_1, k'_2, k_2, k_1) \\ &= \gamma_2(k_1, k_2, k'_1, k'_2)\end{aligned}\tag{2.38}$$

By exploiting these symmetries to the vertex function in the fRG equations, it can be shown that the equations preserve the symmetries.

3. Quantum Point Contacts (QPC)

In this chapter the quantum point contact (QPC) is studied. Firstly, the setup of a QPC and its use to observe one-dimensional transport is illustrated, afterwards the conductance quantization is addressed within a noninteracting picture. Further, a short overview over the conductance anomaly, as it can be observed within a QPC, and related observations is given. Finally, we address the explanation of the conductance anomaly by Bauer et al. [4], since this is the starting point to understand the results in chapter 5.

3.1. One-dimensional transport through a QPC

A quantum point contact (QPC) is a short, quasi-one-dimensional transport channel between two reservoirs. A picture of an experimental setup is depicted in Figure 3.1. A QPC can be realized in a two-dimensional electron gas (2DEG) in e.g. an AlGaAs/GaAs heterostructure [15]. Metal gates as depicted in Figure 3.1 form a 'split-gate' architecture within this 2DEG. These side and central gates, marked with s and c respectively, establish a barrier potential which constricts the transport channel in y-direction. The two reservoirs are source and drain reservoirs and an applied source-drain voltage leads to transport through the contact. Due to the spatial confinement within the contact, there are discretized energy levels. The top gate is used to deplete the 2DEG, such that the number of occupied transversal modes can be assigned.

If one assumes an adiabatically changing potential barrier within the contact that confines the electrons in y-direction, one can consider the transport analogous to transport through a waveguide with locally flat and parallel walls [16]. This leads to the same discretized transverse modes as in a waveguide with a rectangular cross-section, with a width l_y and a height l_z .

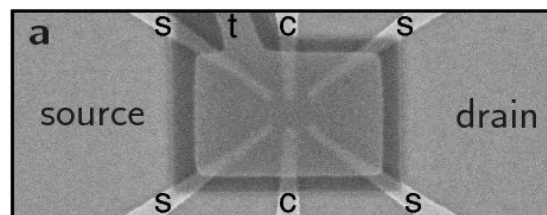


Figure 3.1.: Picture of experimental setup of a quantum point contact. Within a 2DEG metal gates form a 'split-gate' architecture in between source and drain reservoir. Side and central gates can be biased such that they establish a barrier potential which forms a constriction i.e a quasi one-dimensional transport channel. An applied source drain voltage leads to transport through this contact. Top gate voltage controls the depletion of the 2DEG and thus assigns the contributing transport channels. Taken from [4]

The wave function of the electrons can be written:

$$\Psi_n(x, y, z) = \Psi_{n_y}(x, y)\Phi_{n_z}(z). \quad (3.1)$$

The z-dependence can be separated and l_z considered as constant, since only the lowest energy mode is occupied ($n_z = 1$). The Schrödinger equation for $\Psi(x, y)$ then is:

$$\left(-\frac{\hbar^2}{2m} \frac{\partial^2}{\partial x^2} - \frac{\hbar^2}{2m} \frac{\partial^2}{\partial y^2} + V(x, y) \right) \Psi_{n_y}(x, y) = E_{n_y} \Psi_{n_y}(x, y). \quad (3.2)$$

where $V(x, y)$ is the potential that defines the form of the constriction. It has been shown that a saddle-point potential in the constriction of the form

$$V(x, y) = V_c - \frac{1}{2}m\omega_x x^2 + \frac{1}{2}m\omega_y y^2 \quad (3.3)$$

is an realistic assumption [17]. Here the electrons pass a quadratic potential barrier in direction of propagation and are confined in the transverse direction within a parabolic potential with a width propotional to the width of the constriction. Again the variables can be separated locally because the potential only changes adiabatically. The wave function of free motion in x-direction then fulfills:

$$\left(-\frac{\hbar^2}{2m} \frac{\partial^2}{\partial x^2} + E_{n_y} \right) \psi(x) = \psi(x). \quad (3.4)$$

$E_n(x)$ is the mode dependent energy

$$E_{n_y}(x) = \hbar\omega_y[n_y + 1/2] + V(x, 0). \quad (3.5)$$

and the total energy is

$$E = E_{n_y}(x) + \frac{\hbar^2 k_x^2}{2m}. \quad (3.6)$$

Only those modes with energy $E_{n_y} < E_F$ contribute to the transport through the channel. Via the negative top gate voltage the occupied transversal modes can be adjusted.

3.2. Conductance quantization

Transport through a QPC is considered firstly in a noninteracting picture, since it suffices to understand the crude physics.

We consider the current through the constriction coupled to a left and a right reservoir:

$$I = 2se \sum_n \int_{-\infty}^{\infty} \frac{dk_x}{2\pi} v_x(k_x) T_n(E) [f_L(E(k_x)) - f_R(E(k_x))] \quad (3.7)$$

where for those electrons with $k_x > 0$, i.e. coming from left reservoir it holds $f_L(E(k_x)) \equiv f_F(E(k_x) - \mu_L)$, whereas for electrons with $k_x < 0$, i.e. coming from right reservoir $f_R(E(k_x)) \equiv f_F(E(k_x) - \mu_R)$. If one inserts $v_x = \frac{1}{\hbar} \frac{\partial E}{\partial k_x}$ and defines $G_Q = \frac{2e^2}{h}$ as the conductance quantum, it leads to

$$I = \frac{G_Q}{e} \sum_n \int dE T_n(E) [f_L(E) - f_R(E)]. \quad (3.8)$$

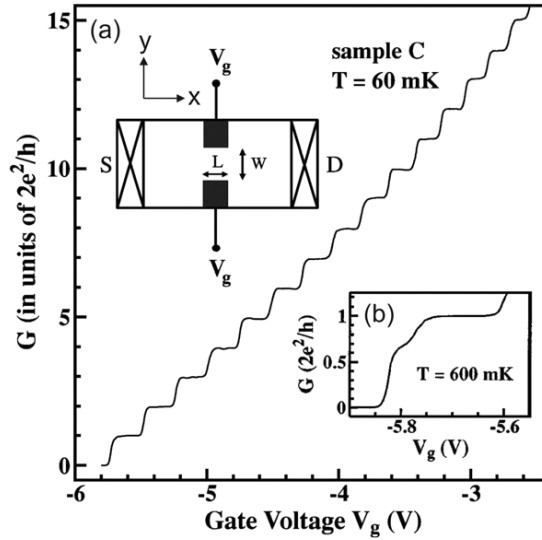


Figure 3.2.: Measurement of the linear differential conductance $G = \frac{dI}{dV}$ as a function of gate voltage. Equal and equidistant plateaus are observed. Inset sketch (a) shows the schematic setup of the QPC, where S and D indicate source and drain reservoir respectively and the black boxes indicate metal gates charged with voltage V_g and thus adjust the passing modes. Inset (b) shows the first plateau which reveals a kink, the so-called 0.7 anomaly. Taken from [18]

Assuming that the transmission T_n is either 1 or 0 for an open or closed channel, respectively, it simplifies to

$$I = \frac{G_Q}{e} N_{open} (\mu_L - \mu_R) = G_Q N_{open} V_{sd}. \quad (3.9)$$

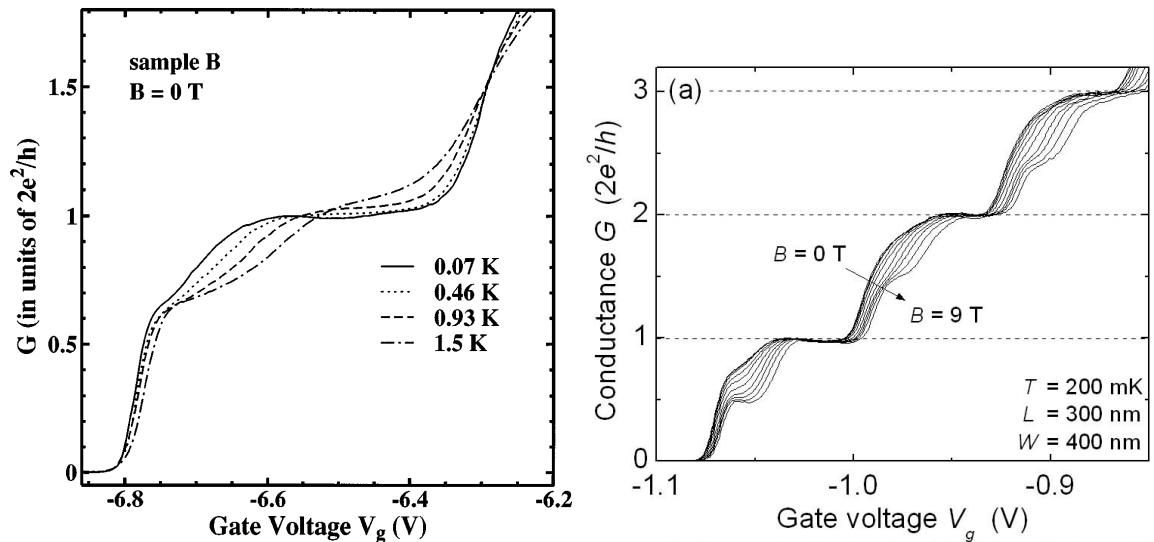
V_{sd} is the source drain voltage, not to be confused with the gate voltage.

Measuring the linear differential conductance $G = \frac{dI}{dV_{sd}}$ as a function of the applied gate voltage V_g one observes plateaus with equal height at equal steps of gate voltage, a staircase of plateaus. Each plateau is an integer multiple of $G_Q = 2e^2/h$, where the conductance increases with increasing gate voltage as shown in Figure 3.2. This has been observed for the first time by van Wees et al. [1] and simultaneously by Wharam et al. [2] in 1988.

One can now easily understand this quantization of conductance. It can be explained in a rather simple single particle picture without any interaction between the electrons using eq.(3.9). By decreasing the gate voltage the 2DEG becomes more and more depleted and less transversal modes are occupied, i.e. less modes contribute to the conductance. Since the conductance is proportional to number of open channel times conductance quantum, one can directly read off the number of open channels. Thus, with each lower plateau one further channel has been closed. This means that one can adjust the number of open channels and this way assign the conductance.

3.3. Conductance anomaly

But a close look on the first plateau, as it is shown in the inset of Figure 3.2, reveals the fact that this does not explain the whole physics. One can see that the first plateau shows



- (a) Evolution with increasing temperature of the first step of the differential conductance measured as a function of gate voltage. It can be seen that the general step structure flattens with rising temperature. But the first step shows different behaviour where the kink becomes more pronounced and the inclination until this kink only changes slightly with temperature. Taken from [3].
- (b) Evolution with increasing magnetic field of the first three steps of the differential conductance measured as a function of gate voltage. It is observed that the shoulder deepens with the magnetic field. With high magnetic field the first three steps evolve into six spin-resolved plateaus. Taken from [19].

Figure 3.3.: Evolution of the conductance with increasing temperature and increasing magnetic field.

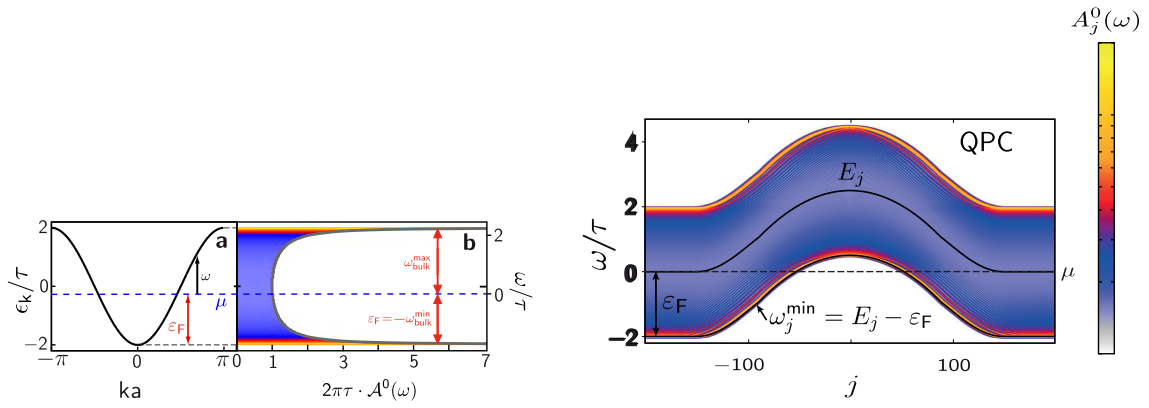
a kink at $G \simeq 0.7G_Q$. This phenomenon has caught the interest in 1996 for the first time, when Thomas et al. [3] addressed this problem. The anomaly and the related observations became famous due to the appearance around a value of $G/G_Q = 0.7$ famous as the '0.7 anomaly'.

Thomas et al. made three important observations about it. Firstly, the kink strengthens with increasing temperature. In Figure 3.3a one can see that while increasing temperature flattens the step structure of the plateaus, the first step behaves differently. Here the kink becomes more pronounced but the lower part of the step changes its inclination only slightly, the step stays as sharp as it is. The fact that above the kink the steps become less sharp with rising temperature can be explained via eq. (3.8). The Fermi function broadens with rising temperature and therefore the energy range of the integral becomes bigger which broadens the steps of the conductance. But the behaviour of the kink in the first step is counterintuitive.

Secondly, increasing the in-plane magnetic field strengthens the shoulder and leads for high magnetic fields to the first spin-resolved plateau where the spin degeneracy is lifted (Figure 3.3b). The lifted spin degeneracy can also be observed in higher conductance steps.

And thirdly, they measured an enhanced g-factor at the first plateau. This is a good indicator that interaction causes the shoulder and that the enhanced interactions are the reason why the 0.7 feature shows up only at the first step.

All these observations have led to a lively debate about the origin of the 0.7 anomaly. While



(a) Dispersion relation and resulting spectral function of a tight-binding chain. The spectral function shows two van Hove singularities. While the upper one is a feature of the model and of no further importance, the lower one is characteristic for a one-dimensional system. Taken from [4]

(b) Resulting band and spectral function shifted by the barrier potential with respect to site j . Colour bar indicates height of spectral function. Taken from [4]

Figure 3.4.: Dispersion relation and density of states of a tight-binding model and the density of states within the band shaped by a barrier potential.

all possible explanations agree that the electron-electron interaction causes this phenomenon, there have been very different approaches to explain it.

3.4. 0.7 anomaly as an interaction effect

An explanation of the 0.7 anomaly has recently been found by Bauer et al. [4]. They show that the phenomenon can be understood as a consequence of the renormalization of the potential due to the great interactions between the electrons within the constriction of the QPC and state that the smeared van Hove singularity of an one-dimensional system is the origin of this anomaly.

They use a tight-binding chain with a parabolic barrier potential with curvature Ω_x to model the QPC. A tight-binding model has two van Hove singularities as depicted in Figure 3.4a. While the lower one is the characteristic van Hove singularity of an one-dimensional system, the upper one is an artefact of the model and of no further importance. With the applied potential barrier of a quantum point contact the local density of states deforms with the potential as illustrated in figure (3.4b). Bauer et al. show that the relevant singularity is cut off due to the missing translational invariance and that the peak is asymmetric with respect to its maximum. Further they point out that the maximum is not at the energy of the barrier height but shifted by an amount of Ω_x , as illustrated in Figure 3.5.

With decreasing barrier, transport channels open up and conductance can be measured. As described above in a noninteracting picture we would expect that the conductance unifor-

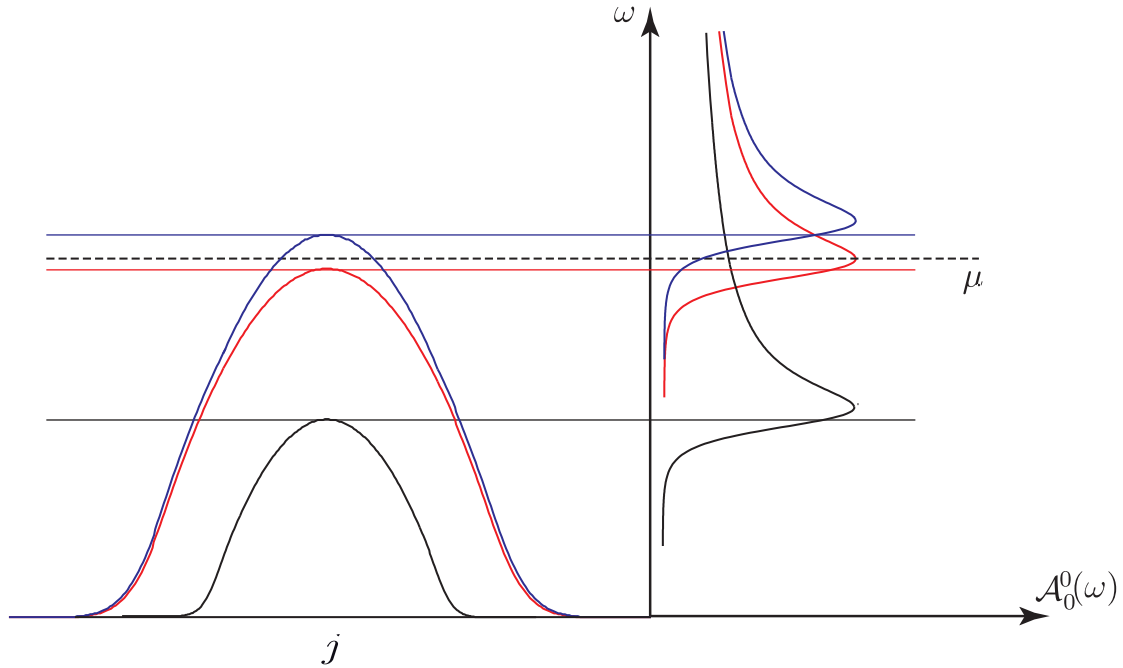


Figure 3.5.: Barrier potential and corresponding peak of the spectral function in the center of the constriction for three different heights of the barrier. Dashed line indicates the chemical potential and coloured solid line indicate position of corresponding barrier top. It is illustrated that the maximum of the peak is shifted with respect to the top of the barrier. Further it can be seen that the change in the local density n is more dramatically if the peak is around the chemical potential (red line) than far away of it (blue and black cases).

mally rises and one would measure a symmetric step of the form

$$G/G_Q = \frac{1}{e^{2\pi(V_g - \mu)/\Omega_x} + 1}. \quad (3.10)$$

where Ω_x is the curvature of the barrier potential and μ the chemical potential. This noninteracting conductance is depicted in Figure 3.7a.

But interaction plays a crucial role. As the interaction of two electrons with each other is proportional to their overlap integral, within the constriction the interaction is strongly enhanced due to the tight transversal potential. This strong interaction leads to two effects that renormalize the effective potential. Even all their calculations are made within the fRG scheme, thus far beyond first order perturbation theory, they can already explain the anomaly by considering a first order self-energy.

Due to the repelling interactions between the electrons the potential becomes renormalized, which in terms of perturbation theory can be written as

$$\tilde{V}_j = V_j + \Sigma_j \quad (3.11)$$

with the first order self-energy

$$\Sigma_j = n_j U_j. \quad (3.12)$$

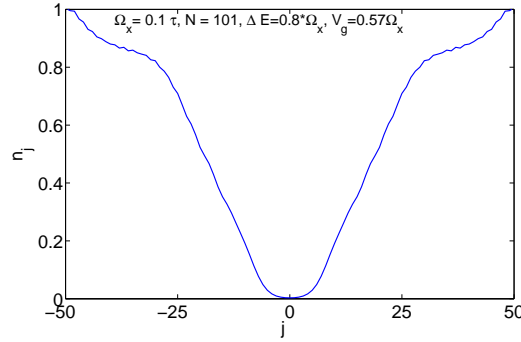


Figure 3.6.: Local density plotted as a function of the site number for a gate voltage above the point where the maximum of the potential passes the chemical potential. Hence, the density is zero in the center and rises towards the leads, because the potential decreases. The Hartree effect is therefore higher where the potential is low. The oscillations are Friedel oscillations and the second slope in the outer region arises because here the potential is so low that the influence of the interaction on the density dominates.

Consequently, this Hartree effect leads to an effectively higher potential at every site with an increasing impact due to an increasing n . Since the local density on each site is given by

$$n_j = \int_{-\infty}^{\mu} A_j^0(\omega) d\omega \quad (3.13)$$

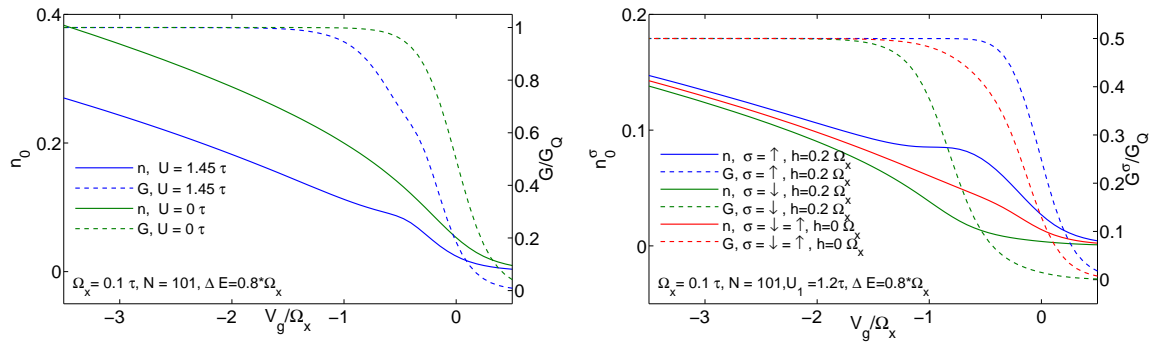
one can see in Figure 3.6 that in general at sites with low potential the local density and thus the impact of this effect is bigger than at those with a high potential. But more important for the characteristic form of the conductance step is the change of the local density with changing gate voltage. In Figure 3.5 three different positions of the barrier height and the corresponding lower peak of spectral function at the central site $j = 0$ are depicted, which illustrates the following relation

$$\frac{dn_j}{dV_g} \propto -A_j^0(\mu) \quad (3.14)$$

i.e. that the change in n with changing gate voltage is more drastically if the peak of the density of states is around the chemical potential than far away of it.

This in mind, one considers the local density at the central site, as depicted in Figure 3.7a. Here the density and the corresponding conductance are plotted as a function of gate voltage with and without interaction. One can see that the density with interaction is always lower due to an effectively higher potential. Further for a certain range of gate voltage the density's increase is considerably less compared to the noninteracting case. The Hartree effect seem to compensate partly the decreasing barrier potential in this domain. It happens when the gate voltage is reduced such that the peak of the DOS passes the chemical potential, which enhances the local density exceedingly. At the same time the higher local density amplifies the Hartree effect, which counteracts and thus compensates partly the rise. The density increases less, a kink arises. The impact on the conductance is accordingly, it can be seen precisely that the increase is less than in the noninteracting case which leads to the pronounced shoulder.

There is a second effect which can be considered as a scattering effect. This effect becomes relevant when the maximum of the DOS lies exactly at the chemical potential. A lot of



- (a) Local density and corresponding conductance as a function of gate voltage with and without interaction. Zero point of the gate voltage corresponds to barrier top at chemical potential. Interaction lowers the local density due to the effectively higher potential. When the peak of the spectral function passes the chemical potential the local density in the interacting case increases less, because the Hartree effect partly compensates the exceeding increase in the local density of states. Thus a kink in the density arises. This has the same impact on the slope of the conductance, there is a pronounced kink in the step. Further, the whole step is shifted due to the higher effective potential.
- (b) Spin resolved local density and corresponding conductance as a function of gate voltage compared to the density and conductance without magnetic field. Zero point of the gate voltage corresponds to barrier top at chemical potential. Effective potentials of the spin up and spin down electrons are shifted apart, because the effective Hartree effect for spin up electrons is decreased for spin down electrons increased. Therefore, their effective potentials pass at very different gate voltages the chemical potential, i.e. while the local density of the spin down electrons firstly show only slight increase, the local density of the spin up electrons rises exceedingly, because its effective potential is already around the chemical potential. The impact on the conductance is accordingly, the shoulder is more pronounced for the spin up electrons, while the conductance of the spin down electrons rises considerably later.

Figure 3.7.: Local density and conductance as a function of gate voltage for the central site.

possible states at the Fermi level then enhance the possibility of elastic scattering which further lowers the increase of the conductance.

Recalling that the maximum of the spectral function lies slightly above the barrier height, it becomes apparent that the peak of the DOS passes the chemical potential for slightly higher gate voltages than the barrier height does. Bauer et al. showed that for a gate voltage related to a conductance of around $0.7G_Q$, the peak passes the chemical potential. Thus, the combination of these effects lead to the special form of the first step of the conductance measured as a function of gate voltage, where the increase of the conductance is diminished in a certain range which forms the prominent kink of the 0.7 anomaly.

The evolution of the conductance with increasing magnetic field can be understood as a consequence of the enhanced Landé factor.

It can be explained in terms of a Hartree effect as well: An applied magnetic field shifts the effective potential within the QPC. Electrons with a spin in direction of the magnetic field experience a lower effective potential, electrons with opposite spin an effectively higher one. This also causes a shift of the density of states and therefore causes a higher density n_{\uparrow}

than n_\downarrow as depicted in Figure 3.7b. Due to the repelling interaction between the electrons the incoming spin down electrons experience an even higher potential, because they are repelled by the electrons which are already within the constriction. Altogether this rises the difference in between the effective potentials of spin up and spin down electrons, i.e. enhances the effective g-factor. In terms of perturbation theory this can be understood similarly as described above, where the effective potential of spin down electrons is

$$\tilde{V}_j^\downarrow = V_j^\downarrow + \Sigma_j^\downarrow \quad (3.15)$$

with

$$\Sigma_j^\downarrow = n_j^\uparrow U_j. \quad (3.16)$$

A magnetic field therefore shifts effective potential of spin up and spin down electrons with respect to each other. This increases the total Hartree effect for spin down electrons, whereas for spin up electrons this effect decreases the total Hartree effect. As we can see in Figure 3.7b it leads to a less pronounced shoulder of the conductance of spin up electrons, while the whole step of the conductance of the spin down electrons is clearly shifted towards lower gate voltages due to this effectively higher Hartree effect. Because the increase of Hartree effect for spin down electrons exceeds the decrease for spin up electrons, combined to the total conductance this strengthens the kink with increasing magnetic field.

4. fRG applied to a QPC with n subbands

In this chapter our tight-binding model of a QPC with n subbands is explained, which offers us the possibility to compute n conductance steps and investigate the influence of the higher modes on the conductance. The fRG equations are set up using an approximation developed by Bauer et al [4] within a static fRG2 scheme. Finally, we define the observables that have been computed.

4.1. Model

In order to compute the conductance through a QPC with n contributing transversal modes we model this system with n infinite tight-binding chains. All chains are exposed to quadratic potentials that form the barriers. On-site Coulomb interaction are between electrons on one site as well as between electrons of the same site of different subbands. Interband transitions are excluded in our model. The model consists of a central contact region which is coupled to semi-infinite noninteracting leads on both sides. This is described by the following Hamiltonian with n subbands:

$$\begin{aligned}
 H = & \sum_{j=1}^N \sum_{k=1}^n \left[(E_j^k - \mu)(n_{k\uparrow,j} + n_{k\downarrow,j}) - \sum_{\sigma \in \{\uparrow, \downarrow\}} \tau (d_{k\sigma,j+1}^\dagger d_{k\sigma,j} + h.c.) \right. \\
 & \left. + \sum_{\sigma, \sigma' \in \{\uparrow, \downarrow\}} \sum_{l=1}^n U_j^{k\sigma, l\sigma'} n_{k\sigma,j} n_{l\sigma',j} - \frac{B}{2} (n_{k\uparrow,j} - n_{k\downarrow,j}) \right]. \quad (4.1)
 \end{aligned}$$

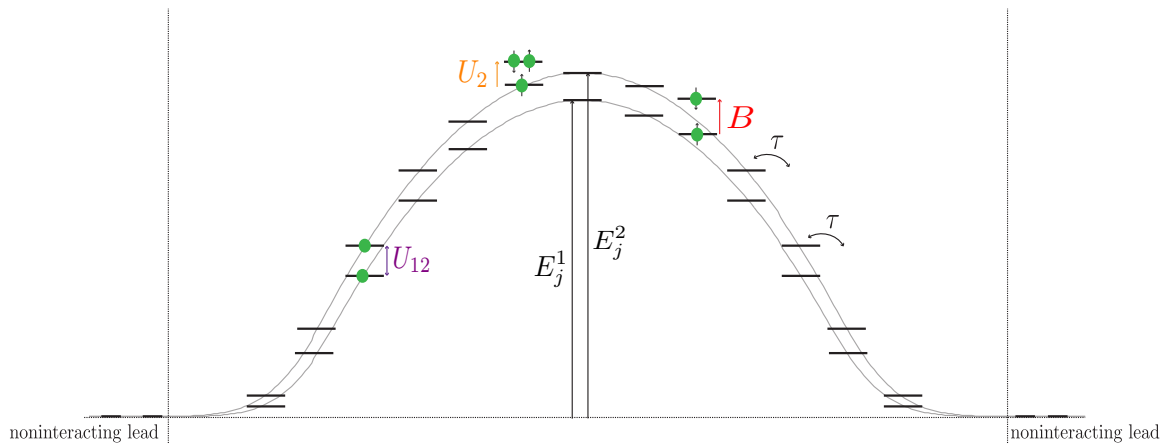


Figure 4.1.: Illustration of the used model for $n = 2$.

$d_{k\sigma,j}^\dagger, d_{k\sigma,j}$ are creation and annihilation operator, respectively and $n_{k\sigma,j}$ is the local density operator where k labels the subband, σ the spin and j the number of site. The first term describes with E_j^k a local potential to model the quantum point contact. The second term specifies the hopping between sites with τ as the hopping amplitude. And the third term describes with $U_j^{k\sigma,l\sigma'}$ the Coulomb interaction, where $U_j^{k\sigma,k\sigma} = 0$ due to Pauli principle. The last term describes Zeeman splitting with B as an external magnetic field. Local potential as well as Coulomb interaction are constricted to the central contact region.

An infinite, homogeneous tight-binding chain is a convenient choice to model a channel through a quantum point contact, since it is applicable to the fRG scheme and shows as discussed in section (3.4) two van Hove singularities, where the one with ϵ_{min} reflects the singularity of a one-dimensional system, whereas the singularity at ϵ_{max} is an artefact of this model which does not do any harm.

Infinity of the chains is modeled by coupling the constriction region to semi-infinite, non-interacting leads on both site. Via projection method one can calculate a lead Green's function g which projects the influence of the semi-infinite chain into the interacting region. For further information about this see [8] or [13]. The noninteracting leads thus are reflected in the Green's function:

$$\mathcal{G}(\omega) = \frac{1}{w - H - \Sigma - g_{lead}(|1\rangle\langle 1| + |N\rangle\langle N|)}. \quad (4.2)$$

As discussed in section 3.1, the potential to model a QPC barrier is a negative quadratic potential. Therefore inside the constriction area it is modeled as follows

$$E_j = \tilde{V}_g - \frac{1}{2}m\omega_x^2 x^2 = \tilde{V}_g - \frac{\Omega_x^2 j^2}{4\tau} \quad (4.3)$$

where the analogy to a harmonic oscillator is used, defining $x = aj$, the mass of electron at the bottom of the energy band $m = \frac{\hbar^2}{2\tau a^2}$ and the curvature of the potential as $\Omega_x = \hbar\omega_x$. Bauer et al. [4] showed that Ω_x defines an energy scale and it is henceforth used as such. Potentials for different subbands are all choosed equal in curvature, but with different offset \tilde{V}_g , such that there is a sublevel spacing $\Delta E = E_{j+1} - E_j$.

The interaction is site-dependent and turned on adiabatically to avoid extra effects due to a sudden rise, since the leads are modeled as noninteracting. Therefore the site dependent factor of the interaction is modeled via

$$U_j = \exp\left(-\frac{((j - 0.5N + 0.5)/2N)^6}{1 - ((j - 0.5N + 0.5)/2N)^6}\right). \quad (4.4)$$

The total interaction then consists of

$$U_j^{k\sigma,l\sigma} = U_j \cdot U_{k\sigma,l\sigma'} \quad (4.5)$$

where the second contribution takes care of the band dependent maximal value of the interaction. $U/\sqrt{\tau\Omega_x}$ defines an effective interaction strength [4], which needs to be chosen carefully in order to avoid divergency, but at the same time cannot be too small to see proper interaction effects.

For the dependence on the subband numbers k and l we consider the following two possibilities. Firstly, a physical assumption is to calculate the overlap of the wave functions which is proportional to the interaction strength. Since we model our constriction with a harmonic potential, the wave functions of a harmonic oscillator can be used to calculate the ratio of interactions. Assuming on-site interactions this leads to

$$U_{k,l} \propto \int_{-\infty}^{\infty} dx |\Psi_k(x)|^2 |\Psi_l(x)|^2 \quad (4.6)$$

with Ψ_k as wave function of the harmonic oscillator. One can calculate e.g. that $U_{2,2} = 0.75 U_{1,1}$ and $U_{1,2} = 0.5 U_{1,1}$. Here we see that the overlap decreases with increasing energy level. As a second possibility, we will also study the case that all interactions are equal. This is at first glance unphysical, but can be used to see possible screening effects in the effective interaction of the higher subbands.

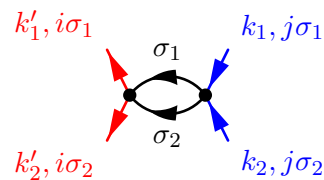
4.2. fRG equations

Starting point are the written out fRG equations for the one- and two-particle vertex functions (eq.(2.34) and (2.35)), because we work in this system with static fRG2. The two-particle vertex functions can be divided into four parts consisting of the three contributions to the vertex function generated by the P -, X - and D - channel plus the bare two-particle interaction U :

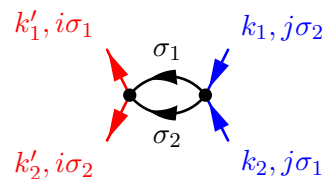
$$\gamma_2^\Lambda = U + \gamma_p^\Lambda + \gamma_x^\Lambda + \gamma_d^\Lambda \quad (4.7)$$

For our calculations we only take those vertices into account which are generated in second order by the bare interaction and set all other vertices to zero. All these vertices and the generating diagrams are depicted below. They are arranged according to their spin and space structure and labeled by the channel in which they are generated most intuitively. It needs to be emphasized that the D - and X - channel are equal up to a minus sign due to an interchange of two legs in the diagram. Therefore, this labeling isn't unique. There are the following types of two-particle vertex functions and their corresponding generating diagrams in second order (black dots denote bare interaction):

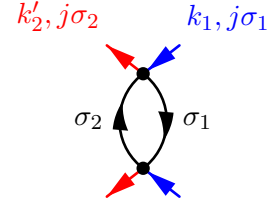
$$P_{ij}^{\sigma_1, \sigma_2} := \gamma_p^\Lambda(i\sigma_1, i\sigma_2; j\sigma_1, j\sigma_2) \quad (4.8)$$



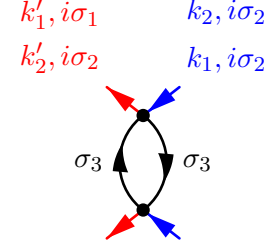
$$\bar{P}_{ij}^{\sigma_1, \sigma_2} := \gamma_p^\Lambda(i\sigma_1, i\sigma_2; j\sigma_2, j\sigma_1) \quad (4.9)$$



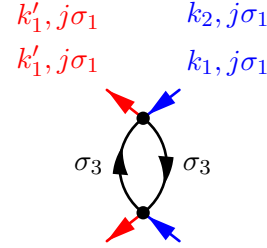
$$X_{ij}^{\sigma_1, \sigma_2} := \gamma_x^\Lambda(i\sigma_1, j\sigma_2; j\sigma_1, i\sigma_2) \quad (4.10)$$



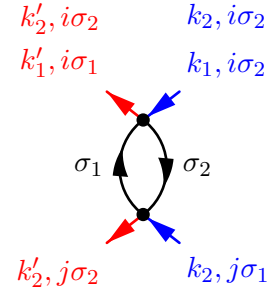
$$\bar{X}_{ij}^{\sigma_1, \sigma_2} := \gamma_d^\Lambda(j\sigma_1, i\sigma_2; i\sigma_2, j\sigma_1) \quad (4.11)$$



$$D_{ij}^{\sigma_1, \sigma_2} := \gamma_d^\Lambda(j\sigma_1, i\sigma_2; j\sigma_1, i\sigma_2) \quad (4.12)$$



$$\bar{D}_{ij}^{\sigma_1, \sigma_2} := \gamma_d^\Lambda(i\sigma_1, j\sigma_2; i\sigma_2, j\sigma_1) \quad (4.13)$$



In order to keep the notation as simple as possible, the subband number is absorbed into the spin number, i.e. instead of using the labels j , k and $\sigma\epsilon(\uparrow, \downarrow)$, we use j and $\sigma\epsilon(1 \uparrow, 1 \downarrow, 2 \uparrow, 2 \downarrow)$.

Time-reversal symmetry of the Hamiltonian leads to

$$\tilde{\mathcal{G}}_{ij}(i\omega) = \tilde{\mathcal{G}}_{ji}(i\omega). \quad (4.14)$$

With this and the symmetries of the two-particle vertex function (as seen in section (2.8)), we get the following symmetries of P , D and X :

$$P_{ij}^{\sigma_1, \sigma_2} = P_{ji}^{\sigma_1, \sigma_2} = P_{ji}^{\sigma_2, \sigma_1} = P_{ij}^{\sigma_2, \sigma_1} = -\bar{P}_{ij}^{\sigma_1, \sigma_2}, \quad (4.15)$$

$$\bar{P}_{ij}^{\sigma_1, \sigma_2} = \bar{P}_{ji}^{\sigma_1, \sigma_2} = \bar{P}_{ji}^{\sigma_2, \sigma_1} = \bar{P}_{ij}^{\sigma_2, \sigma_1} = -P_{ij}^{\sigma_1, \sigma_2}, \quad (4.16)$$

$$X_{ij}^{\sigma_1, \sigma_2} = X_{ji}^{\sigma_1, \sigma_2} = X_{ji}^{\sigma_2, \sigma_1} = X_{ij}^{\sigma_2, \sigma_1} = -\bar{D}_{ij}^{\sigma_1, \sigma_2}, \quad (4.17)$$

$$\bar{X}_{ij}^{\sigma_1, \sigma_2} = \bar{X}_{ji}^{\sigma_1, \sigma_2} = \bar{X}_{ji}^{\sigma_2, \sigma_1} = \bar{X}_{ij}^{\sigma_2, \sigma_1} = -D_{ij}^{\sigma_1, \sigma_2}, \quad (4.18)$$

$$D_{ij}^{\sigma_1, \sigma_2} = D_{ji}^{\sigma_1, \sigma_2} = D_{ji}^{\sigma_2, \sigma_1} = D_{ij}^{\sigma_2, \sigma_1} = -\bar{X}_{ij}^{\sigma_1, \sigma_2}, \quad (4.19)$$

$$\bar{D}_{ij}^{\sigma_1, \sigma_2} = \bar{D}_{ji}^{\sigma_1, \sigma_2} = \bar{D}_{ji}^{\sigma_2, \sigma_1} = \bar{D}_{ij}^{\sigma_2, \sigma_1} = -X_{ij}^{\sigma_1, \sigma_2}, \quad (4.20)$$

If $\sigma_1 = \sigma_2$, it holds

$$D_{ij}^{\sigma, \sigma} = -X_{ij}^{\sigma, \sigma} \quad \text{and} \quad P_{ij}^{\sigma, \sigma} = 0. \quad (4.21)$$

Finally, after exploiting all these symmetries we end up with three different types of vertices, denoted P , X and D , one for each channel. For two subbands for example, i.e. four spin possibilities this leads to 22 different vertex functions.

To set up the differential equations for these vertices, equation (2.35) is splitted into its three parts, following the idea of Bauer [4]. In this way a structure similar to the known random phase approximation structure (RPA) is achieved. Each type of vertex function only generates itself in its corresponding channel, i.e. in that channel in which it has been generated in second order. Those vertex functions, which are generated in higher order in this channel are set to zero. That leads to the following equations:

$$\begin{aligned} \dot{P}_{ij}^{\Lambda, \sigma_1, \sigma_2} &= \dot{\gamma}_p^{\Lambda}(i\sigma_1, i\sigma_2; j\sigma_1, j\sigma_2) \\ &= \frac{1}{2\pi} \sum_{\omega=\pm\Lambda} \sum_{kl} \gamma_2^{\Lambda}(i\sigma_1, i\sigma_2; k\sigma_1, k\sigma_2) \tilde{\mathcal{G}}_{kl}^{\sigma_2, \Lambda}(-i\omega) \tilde{\mathcal{G}}_{kl}^{\sigma_1, \Lambda}(i\omega) \gamma_2^{\Lambda}(l\sigma_1, l\sigma_2; j\sigma_1, j\sigma_2), \end{aligned} \quad (4.22)$$

$$\begin{aligned} \dot{X}_{ij}^{\Lambda, \sigma_1, \sigma_2} &= \dot{\gamma}_x^{\Lambda}(i\sigma_1, j\sigma_2; j\sigma_1, i\sigma_2) \\ &= \frac{1}{2\pi} \sum_{\omega=\pm\Lambda} \sum_{kl} \gamma_2^{\Lambda}(i\sigma_1, k\sigma_2; k\sigma_1, i\sigma_2) \tilde{\mathcal{G}}_{kl}^{\sigma_1, \Lambda}(i\omega) \tilde{\mathcal{G}}_{kl}^{\sigma_2, \Lambda}(i\omega) \gamma_2^{\Lambda}(l\sigma_1, j\sigma_2; j\sigma_1, l\sigma_2), \end{aligned} \quad (4.23)$$

$$\begin{aligned} \dot{D}_{ij}^{\Lambda, \sigma_1, \sigma_2} &= \dot{\gamma}_d^{\Lambda}(j\sigma_1, i\sigma_2; j\sigma_1, i\sigma_2) \\ &= -\frac{1}{2\pi} \sum_{\omega=\pm\Lambda} \sum_{kl} \sum_{\substack{\sigma_3= \\ \text{all spins}}} \gamma_2^{\Lambda}(j\sigma_1, k\sigma_3; j\sigma_1, k\sigma_3) \tilde{\mathcal{G}}_{kl}^{\sigma_3, \Lambda}(i\omega) \tilde{\mathcal{G}}_{kl}^{\sigma_3, \Lambda}(i\omega) \gamma_2^{\Lambda}(l\sigma_3, i\sigma_2; l\sigma_3, i\sigma_2), \end{aligned} \quad (4.24)$$

Eq. (4.23) only holds for $\sigma_1 \neq \sigma_2$, the differential equation of $X_{ij}^{\sigma, \sigma}$ is covered by eq. (4.24).

These equation can be written in a compact matrix notation:

$$\frac{d}{d\Lambda} P^{\sigma_1, \sigma_2} = \tilde{P}^{\sigma_1, \sigma_2} \Pi_p^{\sigma_1, \sigma_2} \tilde{P}^{\sigma_1, \sigma_2}, \quad (4.25)$$

$$\frac{d}{d\Lambda} X^{\sigma_1, \sigma_2} = \tilde{X}^{\sigma_1, \sigma_2} \Pi_x^{\sigma_1, \sigma_2} \tilde{X}^{\sigma_1, \sigma_2}, \quad (4.26)$$

$$\frac{d}{d\Lambda} D^{\sigma_1, \sigma_2} = \sum_{\substack{\sigma_3 = \\ \text{all spins}}} -\tilde{D}^{\sigma_1, \sigma_3} \Pi_d^{\sigma_3, \sigma_3} \tilde{D}^{\sigma_3, \sigma_2}, \quad (4.27)$$

\tilde{P} , \tilde{X} and \tilde{D} are defined as follows:

$$\tilde{P}_{ij}^{\sigma_1, \sigma_2} = P_{ij}^{\sigma_1, \sigma_2} + \delta_{ij} (X_{jj}^{\sigma_1, \sigma_2} + D_{jj}^{\sigma_1, \sigma_2}), \quad (4.28)$$

$$\tilde{X}_{ij}^{\sigma_1, \sigma_2} = X_{ij}^{\sigma_1, \sigma_2} + \delta_{ij} (P_{jj}^{\sigma_1, \sigma_2} + D_{jj}^{\sigma_1, \sigma_2}), \quad (4.29)$$

$$\tilde{D}_{ij}^{\sigma_1, \sigma_2} = D_{ij}^{\sigma_1, \sigma_2} + \delta_{ij} (1 - \delta_{\sigma_1, \sigma_2}) (P_{jj}^{\sigma_1, \sigma_2} + X_{jj}^{\sigma_1, \sigma_2}) - \delta_{ij} \delta_{\sigma_1, \sigma_2} D_{ij}^{\sigma_1, \sigma_2}, \quad (4.30)$$

The side diagonal term of \tilde{P} , \tilde{X} and \tilde{D} takes into account the fact that

$$\gamma_2^\Lambda(j\sigma_1, j\sigma_2; j\sigma_1, j\sigma_2) = U_j^{\sigma_1, \sigma_2} + P_{jj}^{\sigma_1, \sigma_2} + X_{jj}^{\sigma_1, \sigma_2} + D_{jj}^{\sigma_1, \sigma_2} \propto \delta_{\sigma_1, \sigma_2} \quad (4.31)$$

i.e. that more than one channel contributes to this vertex function in second order and in eq.(4.30) the last term uses eq.(4.21) and thereby ensures Pauli principle.

The bubbles for the P - and X/D -channel are defined in the following manner, respectively:

$$\Pi_{p,kl}^{\sigma_1, \sigma_2} = \sum_{\omega=\pm\Lambda} \tilde{\mathcal{G}}_{kl}^{\sigma_1, \Lambda}(-i\omega) \tilde{\mathcal{G}}_{kl}^{\sigma_2, \Lambda}(i\omega) = \sum_{\omega=\pm\Lambda} \tilde{\mathcal{G}}_{kl}^{\sigma_1, \Lambda}(i\omega) \tilde{\mathcal{G}}_{kl}^{\sigma_2, \Lambda}(-i\omega), \quad (4.32)$$

$$\Pi_{x,kl}^{\sigma_1, \sigma_2} = \Pi_{d,kl}^{\sigma_1, \sigma_2} = \sum_{\omega=\pm\Lambda} \tilde{\mathcal{G}}_{kl}^{\sigma_1, \Lambda}(i\omega) \tilde{\mathcal{G}}_{kl}^{\sigma_2, \Lambda}(i\omega) \quad (4.33)$$

where σ_1 and σ_2 can take any possible spin value. The differential equation for the self-energy and accordingly the one-particle vertex function can be written in the following way starting from eq.(2.34):

$$\begin{aligned} \frac{d}{d\Lambda} \Sigma_{ji}^{\sigma_1, \Lambda} &= -\dot{\gamma}_1^\Lambda(j\sigma_1; i\sigma_1) \\ &= -\frac{1}{2\pi} \sum_{\omega=\pm\Lambda} \sum_{\sigma_2 \neq \sigma_1} \tilde{\mathcal{G}}_{ji}^{\sigma_2, \Lambda}(i\omega) P_{ij}^{\sigma_1, \sigma_2} + \tilde{\mathcal{G}}_{jj}^{\sigma_2, \Lambda}(i\omega) U_j^{\sigma_1, \sigma_2} \delta_{ij} + \tilde{\mathcal{G}}_{ji}^{\sigma_2, \Lambda}(i\omega) X_{ij}^{\sigma_1, \sigma_2} \\ &\quad + \delta_{ij} \sum_k \tilde{\mathcal{G}}_{kk}^{\sigma_2, \Lambda}(i\omega) D_{jk}^{\sigma_1, \sigma_2} - \tilde{\mathcal{G}}_{ji}^{\sigma_1, \Lambda}(i\omega) D_{ij}^{\sigma_1, \sigma_1} (1 - \delta_{ij}) \\ &\quad + \delta_{ij} \sum_{k \neq j} \tilde{\mathcal{G}}_{kk}^{\sigma_1, \Lambda}(i\omega) D_{jk}^{\sigma_1, \sigma_1} \end{aligned} \quad (4.34)$$

where eq. (4.31) has been used and the fact that

$$\gamma_2^\Lambda(j\sigma, j\sigma; j\sigma, j\sigma) = 0 \quad (4.35)$$

due to Pauli principle.

Initially, we set all vertex functions to zero:

$$P_{ij}^{\sigma_1, \sigma_2, \Lambda_i} = X_{ij}^{\sigma_1, \sigma_2, \Lambda_i} = D_{ij}^{\sigma_1, \sigma_2, \Lambda_i} = 0 \quad (4.36)$$

Here Λ_i is the initial value of flow parameter Λ .

4.3. Observables

4.3.1. Conductance

Our main goal is to compute the transport through the interacting system of a QPC. In order to compute the conductance we use the Landauer-Büttiker formula, which a priori is only valid within a noninteracting model. But it has been shown that it is valid for interacting systems within the fRG scheme. Thus, the formula is just quoted here, for a detailed explanation, see [9].

$$G = \frac{e^2}{h} \sum_{\sigma} |2\pi \rho_{lead}(\mu) \tau_1^L \tau_N^R \mathcal{G}_{N,1}^{\sigma}(\mu)|^2 \quad (4.37)$$

where ρ_{lead} is the density of states of the noninteracting leads and τ are the coupling constants to the leads.

4.3.2. Local density

Another physical observable which is computed is the local density, also called local charge, which is composed of the spin resolved local density as

$$n_j = n_{j\uparrow} + n_{j\downarrow}. \quad (4.38)$$

As already used in section (3.4) the local density can be written as

$$\begin{aligned} n_j^{\sigma} &= \int_{-\infty}^{\mu} A_j^{\sigma}(\omega) d\omega \\ &= -\frac{1}{\pi} \int_{-\infty}^{\mu} \text{Im} \mathcal{G}_{jj}^{\sigma}(\omega) d\omega \end{aligned} \quad (4.39)$$

for $T=0$ [[20], section 11.4.2]. On the other hand,

$$n_j^{\sigma} = \langle c_{j,\sigma} c_{j,\sigma}^{\dagger} \rangle = \frac{1}{\beta} \sum_n \mathcal{G}_{jj}^{\sigma}(i\omega_n) e^{i0^+} \quad (4.40)$$

and it can be shown that the convergence factor leads to an extra factor of $\frac{1}{2}$ [21]

$$n_j^\sigma = \frac{1}{\beta} \sum_{\omega_n \geq 0} \text{Re} \mathcal{G}_{jj}^\sigma(i\omega_n) + \frac{1}{2} \quad (4.41)$$

which is the used equation to compute it numerically.

Because we use static fRG, we are forced to set up the frequency dependent Green's function with the frequency independent self-energy computed in our fRG scheme. This seems to be a crude approximation, but it has been shown by Andergassen et al. [5] that this leads to good and reliable results.

4.3.3. Local magnetization

The local magnetization is computed from the local density via

$$m_j = \frac{1}{2}(n_{j,\uparrow} - n_{j,\downarrow}). \quad (4.42)$$

4.3.4. Spin susceptibility

The local spin susceptibility is computed as

$$\chi_j = \left(\frac{\partial m_j}{\partial B} \right)_{B=0}, \quad (4.43)$$

the total spin susceptibility

$$\chi_{tot} = \sum_j \chi_j \quad (4.44)$$

with the sum over the central contact region.

4.3.5. Low-energy scale B^*

For a fixed gate voltage the conductance can be described in dependence of magnetic field B , temperature T and source drain voltage V_{sd} as [4]

$$\frac{G(B, T, V_{sd})}{G_Q} \simeq 1 - \frac{B^2}{B^{*2}} - \frac{T^2}{T^{*2}} - \frac{V_{sd}^2}{V_{sd}^{*2}}. \quad (4.45)$$

Since we work with static fRG, we can access neither the influence of nonzero temperature nor of the source drain voltage, but only of the magnetic field. Thus, we only consider the dependence on the magnetic field of the conductance

$$\frac{G(B)}{G_Q} \simeq 1 - \frac{B^2}{B^{*2}}. \quad (4.46)$$

By computing B^* the strength of the influence of the magnetic field on conductance is evaluated. The smaller the energy scale B^* the stronger the influence of the magnetic field.

5. Results

The model of a QPC with n subbands as presented in section 4.1 is used within the fRG scheme to investigate the impact of higher modes on the conductance and the 0.7 anomaly. The numerically computed results are presented in this chapter. Firstly, our model and the corresponding fRG equations offer the possibility to investigate the effect of one third order term in the fRG equations on the conductance of a one-band model. To investigate the impact of more than one transport channel on the conductance anomaly, systems with two subbands and with four subbands are considered. Finally, the impact of one half-filled subband on a second subband is examined.

In all figures in this chapter the gate voltage as defined in (4.3) is shifted by half the bandwidth 2τ :

$$V_g = \tilde{V}_g - 2\tau. \quad (5.1)$$

This way the zero point denotes the gate voltage where the barrier top is at the chemical potential. Further, the hopping amplitude is chosen constant throughout the whole thesis and set to one, i.e. $\tau = 1$.

5.1. Effect of one higher order term on the conductance of a one-band model

If one looks at the fRG equations as set up in section 4.2, one can consider the vertex functions of a model with two or more subbands and compare them with the vertex functions which are generated in second order in a one-band model. In equations (4.8) to (4.12) the different types of vertices and their generating diagrams are shown. Vertex functions denoted as $P_{i,j}^{\sigma_1,\sigma_2}$ and $X_{i,j}^{\sigma_1,\sigma_2}$ can be generated in a one-band model the same way, but the vertex function denoted as $D_{i,j}^{\sigma_1,\sigma_2}$ is generated in second order only for $\sigma_1 = \sigma_2$. Looking at equation (4.12) and its corresponding diagram this is easy to understand. For a second order diagram there needs to be a third possible number in σ if σ_1 and σ_2 are different, because there is no interaction between electrons in the same state due to Pauli principle. Recalling that the quantum number σ is a composite index for both the spin and the band number, we can easily see that for a one-band model there are only spin up and spin down, i.e. two possibilities for σ . Therefore the diagram of eq.(4.12) is not possible in a one-band model if $\sigma_1 \neq \sigma_2$, because it requires at least three different spin-band-states. But the corresponding vertex function is generated in third order in a one-band model.

Our equations are set up to consider a two-band model, but setting $U_2 = U_{12} = 0$ we can take the equations for the one-band model as well. Further we can either set the extra third order $D_{i,j}^{\sigma_1,\sigma_2}$ vertex artificially to zero or take it into account and this way we can see its influence on the full interaction.

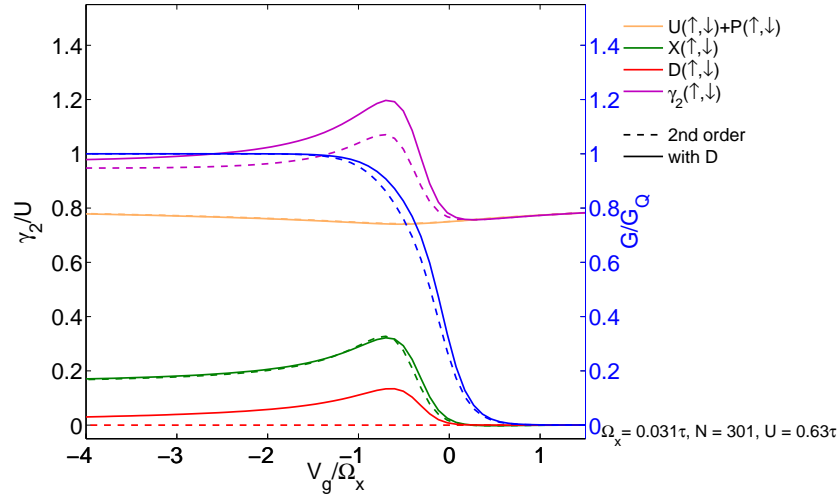
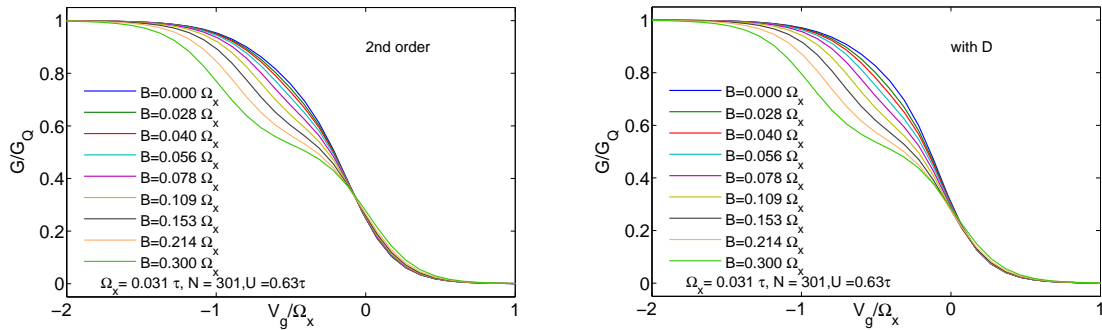


Figure 5.1.: Comparison of vertex functions at the central site and conductance plotted against gate voltage for one band. The dashed lines denote the purely second order model, the solid lines the model with $D_{0,0}^{\uparrow,\downarrow}$. The $D_{0,0}^{\uparrow,\downarrow}$ is positive and therefore enhances the effective interaction. Its effect on $P_{0,0}^{\uparrow,\downarrow}$ and $X_{0,0}^{\uparrow,\downarrow}$ is small, while it causes the conductance shoulder to become less pronounced.



(a) Conductance as a function of gate voltage for several values of B for the purely second order model of one band. (b) Conductance as a function of gate voltage for several values of B for a one-band model with the third order vertex function $D_{0,0}^{\uparrow,\downarrow}$.

Figure 5.2.: Comparison of the conductance as a function of gate voltage for several values of a magnetic field B for the purely second order model and the one with the extra D structure. With increasing magnetic field the kink becomes more pronounced. Its effect is even stronger with $D_{0,0}^{\uparrow,\downarrow}$ nonzero, in agreement with the higher effective interaction (see Figure 5.1). In the purely second order model the lower part of the step is more faded out.

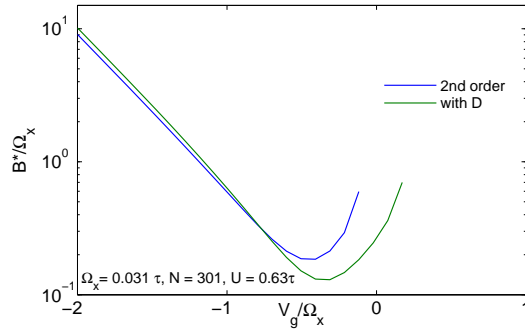


Figure 5.3.: Low-energy scale B^* logarithmic plotted as a function of gate voltage, computed with and without the extra $D_{0,0}^{\uparrow,\downarrow}$ structure. B^* shows a negative exponential dependence on the gate voltage for $V_g < -0.4\Omega_x$. The extra D structure leads here to a shift of the curve towards higher gate voltage and between $V_g = 0\Omega_x$ and $V_g = -0.8\Omega_x$ to a smaller B^* , thus an increased impact of the magnetic field.

In Figure 5.1 the results are compared. The different contributions to the full vertex function at the central site of the potential and the conductance as a function of gate voltage are depicted. Dashed lines are used for the purely second order model, solid lines for a model with the third order $D_{i,j}^{\sigma_1,\sigma_2}$ structure. The vertex functions $P_{0,0}^{\uparrow,\downarrow}$, $X_{0,0}^{\uparrow,\downarrow}$ and $D_{0,0}^{\uparrow,\downarrow}$ are defined in eq.(4.8) to (4.12) with $n=1$ and sum up to the full vertex function γ_2 (eq.(4.31)). All values are considered for $i = j = 0$, i.e. at the central site of the chain.

We can see that the $D_{0,0}^{\uparrow,\downarrow}$ vertex is positive and adds up such that the full vertex γ_2 is enhanced. It is smaller than the contribution of the two other structures, as expected for a higher order term. There is an influence on the $P_{0,0}^{\uparrow,\downarrow}$ and $X_{0,0}^{\uparrow,\downarrow}$ structure due to the fact that for diagonal term as by definition (4.28, 4.29, 4.30) the vertex functions of different channels contribute to each other. But this influence is rather small. The conductance with the $D_{0,0}^{\uparrow,\downarrow}$ function rises slightly quicker and therefore shows a less pronounced shoulder.

In Figures 5.2a and 5.2b the evolution of the conductance with rising magnetic field is illustrated without and with $D_{0,0}^{\uparrow,\downarrow}$ respectively. One can see the expected enhancement of the kink with rising magnetic field. Though the conductance step with zero magnetic field shows a less pronounced shoulder with nonzero $D_{0,0}^{\uparrow,\downarrow}$, the influence of the magnetic field is enhanced, especially for small magnetic fields. This is in agreement with the higher effective interaction in Figure 5.1, since the interaction increases the effective Landé factor. Further it can be observed that the lower tail is more fanned out for the purely second order model than with the extra D structure.

These observations are confirmed, if the low-energy scale B^* is considered. It is a quantity that measures the impact of the magnetic field and defined via eq. (4.46). In Figure 5.3 the dependence of B^* with respect to the gate voltage is depicted for a purely second order model and with the extra D structure. B^* shows a negative exponential dependence on the gate voltages if $V_g < -0.4\Omega_x$. If the extra D structure is included the curve becomes shifted towards higher gate voltages. Between $V_g = 0\Omega_x$ and $V_g = -0.8\Omega_x$ B^* is smaller, accordingly the effect of the magnetic field is enhanced, as observed above. Below $V_g = -0.8\Omega_x$ the energy scale B^* is slightly higher if $D_{0,0}^{\uparrow,\downarrow}$ is included, the influence of the magnetic field decreased.

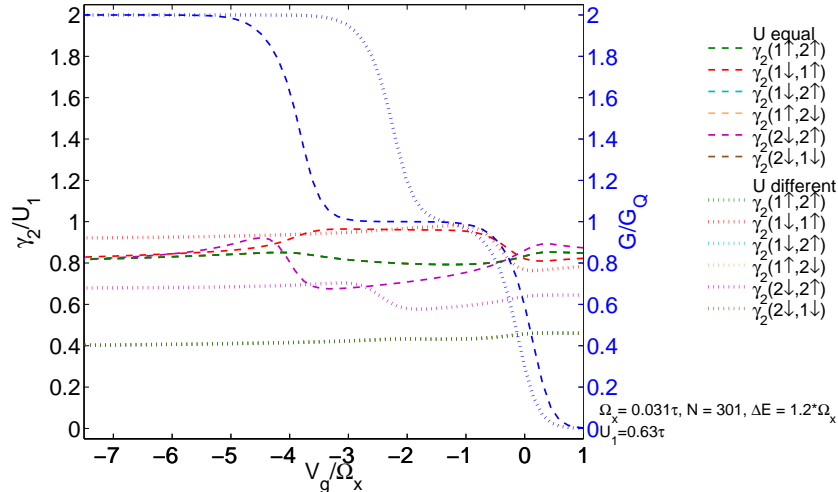


Figure 5.4.: Comparison of conductance and vertex functions on the central site for two different choices of the interaction plotted as a function of gate voltage. The width of the plateau is much bigger if the interactions are chosen equal than if the interactions are chosen as in eq. (5.2). In both cases the shape of the steps appear equal. Vertex function on the central site are depicted in units of the on-site interaction of the first mode. Overall behaviour is equal in both cases, but the vertex functions in the case of equal interactions are bigger due to the bigger interactions. Further they show more pronounced maxima and minima and as the conductance they are shifted towards smaller gate voltage. Only the vertex function of the first mode $\gamma_2(1 \uparrow, 1 \downarrow)$ shows a pronounced difference. In case of equal interactions it decreases, when the second step of conductance starts to rise and thus becomes smaller than the corresponding vertex function in the case of different interactions. Comparing the vertex functions $\gamma_2(1 \uparrow, 1 \downarrow)$ and $\gamma_2(2 \uparrow, 2 \downarrow)$ in case of equal interactions, it is noticed that the vertex function of the second mode has a slightly smaller maximum.

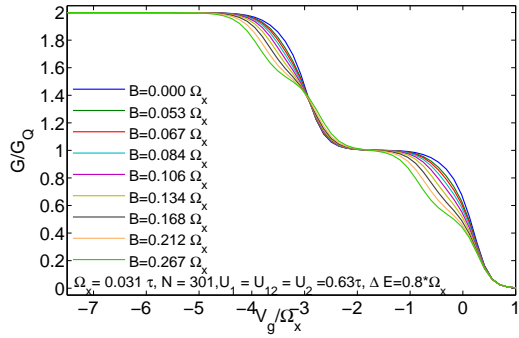
5.2. QPC modelled with two subbands

As presented in section 3.4, Bauer et al. [4] modeled a quantum point contact with one tight-binding chain to compute the first conductance step, where the conductance anomaly of a QPC is observed. Motivated by this work, we now considered the model presented in section 4.1 with n chains, i.e. with n transversal modes to study conductance where more than one mode is involved. We begin by considering a model with two chains.

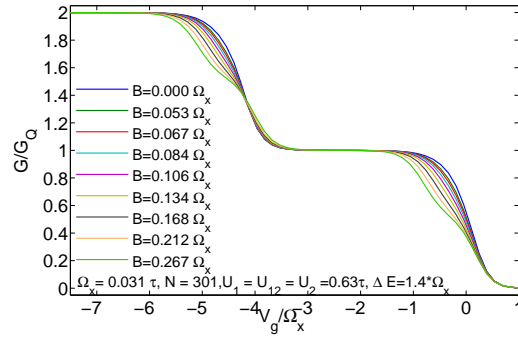
It has been discussed in section 4.1 that it is a physical assumption that the on-site interaction for the first mode is larger than the one in the second mode and in between the modes. Calculated with eq. (4.6), for a two-band model we take

$$U_2 = 0.75 \cdot U_1 \quad \text{and} \quad U_{12} = 0.5 \cdot U_1. \quad (5.2)$$

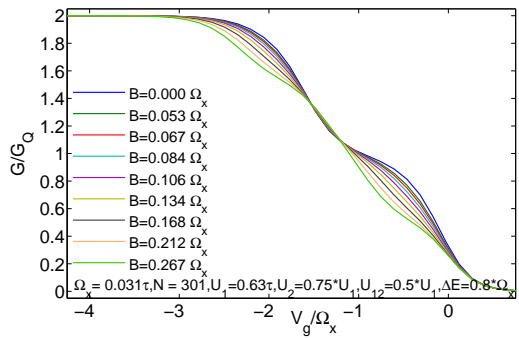
On the other hand, setting all interactions equal, potential screening effects on the effective interaction could be observed. Hence, all observables are computed for these two possible choices of interaction strengths. Throughout this chapter the first choice is denoted as 'with different interaction' and respectively the second one as 'with equal interaction'.



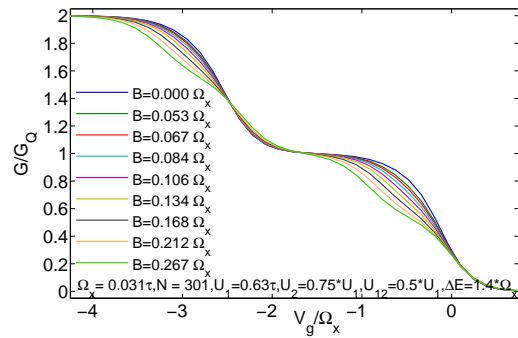
(a) Conductance as a function of gate voltage for several values of magnetic field B for a two-band model with equal interactions with a small subband spacing.



(b) Conductance as a function of gate voltage for several values of magnetic field B for a two-band model with equal interactions with bigger subband spacing.



(c) Conductance as a function of gate voltage for several values of magnetic field B for a two-band model with different interactions with a small subband spacing.



(d) Conductance as a function of gate voltage for several values of magnetic field B for a two-band model with different interactions with a bigger subband spacing.

Figure 5.5.: Conductance as a function of gate voltage for two different sublevel spacings ΔE . Upper row shows conductance with equal interactions, lower row shows conductance with interactions chosen with the ratio of eq.(5.2). Equal interactions lead to a largely elongated conductance step compared to the case of different interactions. The impact of the magnetic field can be seen best in the Figures 5.5a and 5.5d, where one can observe that the change with magnetic field in the second step is larger if $U_2 = U_1$ than if they are chosen differently.

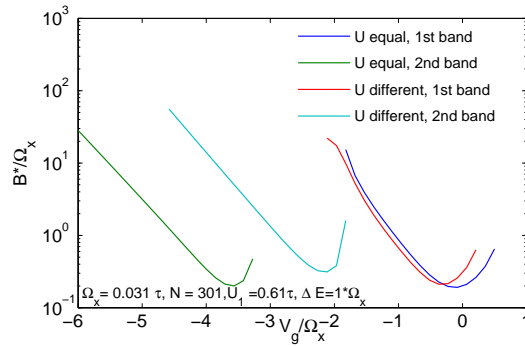
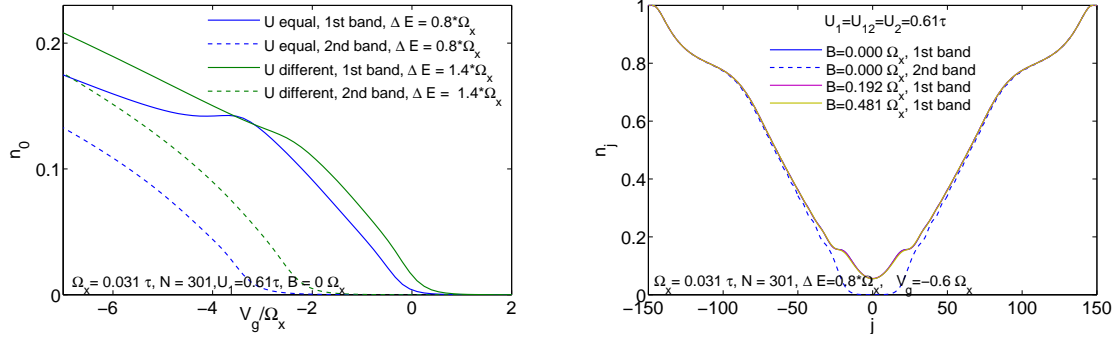


Figure 5.6.: Low-energy scale B^* plotted logarithmically as a function of gate voltage for the first and second subband in the cases of equal and different interactions. B^* shows a negative exponential dependence on the gate voltage. This holds better for the second subbands than for the first bands, where the slope is not perfectly straight. The curve for B^* with equal interactions is slightly shifted towards higher gate voltages. The curves for the second subbands are shifted with respect to each other analogously as the second conductance step. The minimum of B^* for the second band with different interactions lies at a higher value, which reflects the fact, that the influence of the magnetic field is less in the second step as observed in Fig. 5.5d.

In Fig. 5.4 conductance and vertex functions on the central site are plotted as a function of gate voltage for the two choices of interactions. Though the sublevel spacing $\Delta E = 1.2 * \Omega_x$ is equal in both cases and thus one would expect the same plateau width, one notices that the width is much bigger if the interactions are chosen equal than with different interactions. The shape of the conductance steps does not differ, neither in between the different choices of interaction nor in between the first and second step of the same case.

Fig. 5.4 also depicts the vertex functions at the central site in units of the bare interaction U_1 , i.e. the on-site interaction of the first mode. The interaction is chosen as $U_1 = 0.63\tau$. Comparing the vertex function for the two cases of interactions, it is observed that they show nearly equal behaviour. The most pronounced difference is exhibited by the vertex function of the first mode $\gamma_2(1 \uparrow, 1 \downarrow)$, which is the biggest vertex function in both cases. It has a maximum at the gate voltage, where the conductance bends. Further it can be observed that in the case of equal interactions the vertex function decreases when the second step of the conductance starts to rise, while with different interactions it does not decrease that explicitly. Hence, for low gate voltages this vertex function is smaller in the case of equal interactions than with different interactions. The vertex function of the second mode $\gamma_2(2 \uparrow, 2 \downarrow)$ and all vertex functions for interaction between the two modes $\gamma_2(1\sigma, 2\sigma')$ show similar behaviour for both cases. $\gamma_2(2 \uparrow, 2 \downarrow)$ shows a maximum at that gate voltage, where the conductance bends. All $\gamma_2(1\sigma, 2\sigma')$ have the same value, independent of the exact spins and show unexplicit maxima and minima. In the case of different interactions, i.e. with smaller U_{12} and U_2 , the vertex function are accordingly smaller, show less pronounced minima and maxima and they are shifted as the second step of the conductance with respect to the gate voltage. Comparing the vertex functions $\gamma_2(1 \uparrow, 1 \downarrow)$ and $\gamma_2(2 \uparrow, 2 \downarrow)$ in the case of equal interactions, it is noticed that the vertex function of the second mode has a slightly smaller maximum.

In the Figures 5.5 the conductance is plotted as a function of gate voltage and one can see



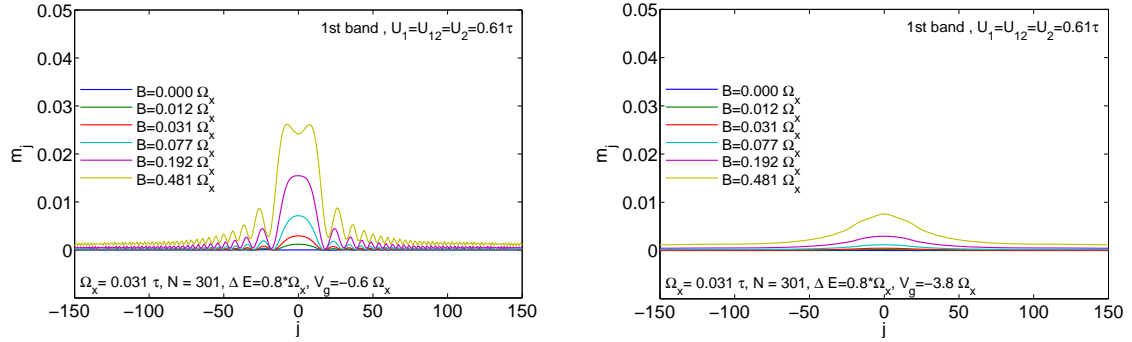
- (a) Local density plotted as a function of gate voltage for the first and second band with equal interactions and different interaction. With decreasing gate voltage the local density rises as the channels open up. When the second subband starts to open up, this has a pronounced effect on the local density of the first subband, the slope decreases. In the case of equal interaction this even leads to a domain of constant density.
- (b) Local density of the first and second subband plotted as a function of site number j for several values of magnetic field B . The gate voltage is chosen such that the first transport channel is open, while the second one is still closed. The minimum of the local density lies at the central site and is nonzero for the first band and zero for the second subband. With decreasing potential towards the leads, the local density increases. The density of the first band is bent, when the local density of the second band starts to rise. In the outer regime the influence of the interaction dominates the impact of the potential, which yields the different slope. A magnetic field does not change the local density of the first band.

Figure 5.7.: Local density as a function of gate voltage (5.7a) and as a function of the number of site j for several values of B (5.7b).

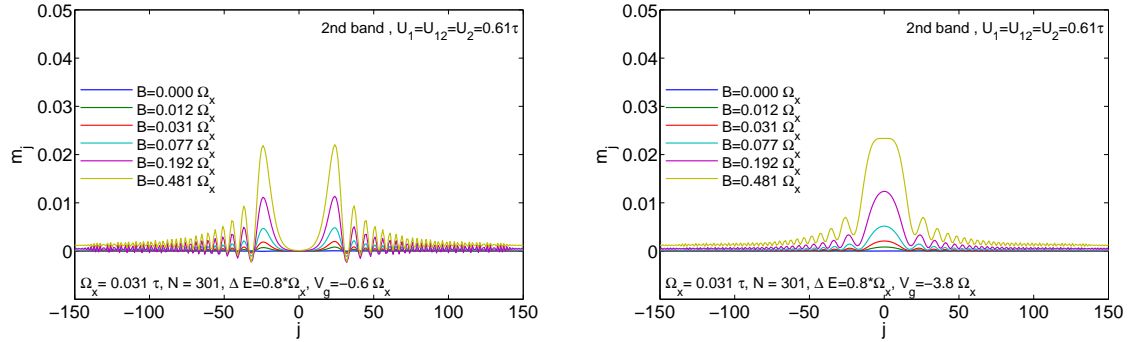
again that the choice of the interaction affects the width of the first plateau. While the whole appearance of the steps with different interactions is a little more elongated than with equal interactions, the plateau is much larger with equal interactions. Therefore, we computed the conductance for two different sublevel spacing $\Delta E = 0.8 \Omega_x$ and $\Delta E = 1.4 \Omega_x$. One can see that in the case of equal interactions the width is very broad with a sublevel spacing of $\Delta E = 1.4 \Omega_x$, hence a better choice is $\Delta E = 0.8 \Omega_x$. On the other hand, for the case where the interaction are chosen via eq. (5.2) a sublevel spacing of $\Delta E = 0.8 \Omega_x$ is too small. When the second channel starts to open, the first step is not saturated yet. In this case a more reasonable choice seems to be a sublevel of $\Delta E = 1.4 \Omega_x$.

The influence of the magnetic field on the conductance can be seen best with reasonable sublevel spacing as in the Fig. 5.5a and Fig. 5.5d. It is equal in the first and the second step in the case of equal interactions, which is consistent with equal interactions in the first and second mode. For different interactions (Fig. 5.5d) it can be noticed that the effect of the magnetic field is larger in the first step than in the second step, which analogously might be explained with the smaller interaction in the second mode. Further one can see that in the second step the lower part is more fanned out in both cases of interaction. This cannot be seen in the first step, there all curves lie above each other in the lower tail of the step.

The influence of the magnetic field can also be read off the low-energy scale B^* . It is depicted



- (a) Local magnetization as a function of the site number j for the first subband. The gate voltage is chosen such that the first channel is open, while the second one is closed. The magnetization has its maximal value at the central region, which enhances with increasing magnetic field. With particular high magnetic field the effective potential for spin down electrons is too high, only spin up electrons can pass which leads to the small dip in the maximum.
- (b) Local magnetization as a function of the site number j for the first subband. The gate voltage is chosen such that both channels are open. Therefore, magnetization is rather small and has its maximum at the central site, which increases with increasing magnetic field.



- (c) Local magnetization as a function of the site number j for the second subband. The gate voltage is chosen such that the first channel is open, while the second one is closed. Thus, in the central region there is no local density independent of the magnetic field. With decreasing potential towards the leads the density increases and therefore the magnetization abruptly rises and then again exponentially decays in the outer regime. The abrupt increase is observed because in this region the magnetic field not only lowers one spin resolved density while enhancing the other, but can lead to an effectively closed channel for spin down where spin up can already pass the constriction. With increasing magnetic field the magnetization rises.
- (d) Local magnetization as a function of the site number j for the second subband. The gate voltage is chosen such that both channels are open. This leads to a maximal magnetization in the central region, which increases with increasing magnetic field.

Figure 5.8.: The local magnetization as a function of the site number j for several values of the magnetic field B and equal interactions. The upper row shows the magnetization for the first subband, the second row the second subband. First column shows the magnetization for a gate voltage that leads to an open first, but closed second channel, while in the second column both channels are open. The oscillations are a consequence of the Friedel oscillations of the local density.

in Figure 5.6 for the first and the second subband and in the case of equal and different interactions. The B^* of the first band shows a very broad minimum compared to the one of the second subband. In case of equal interactions the whole curve is shifted towards lower gate voltages in comparison to the case with different interactions. With decreasing gate voltage B^* rises, but greater as in the second subband and not that straight. The low-energy scale B^* of the second subband shows a perfect straight slope with decreasing gate voltage. The two different curves of the two possible choices of interactions are shifted with respect to each other, as expected since the second steps of the conductance are shifted as well. Further one can see that the minimum of B^* of the second subband in case of different interactions is higher as the minima of the first subband and as the minimum of the second subband in case of equal interactions. This reflects the above discussed observation that the influence of the magnetic field is smaller in the second step if the interactions U_{12} and U_2 are smaller.

In Figure 5.7a the local density (computed via eq. (4.41)) for the central site in the first and second step is compared for the situations with equal and different interactions. It is observed that the density of the first subband with different interactions starts to rise earlier than with equal interactions. Both rise with the same slope. Very pronounced is the effect of the second subband on the local density of the first band. When the second channel opens, the rising local density of the second band leads to a kink in the slope of the density of the first band. In the case of equal interactions this even yields a regime of constant local density. Further it needs to be remarked, that even with nearly doubled sublevel spacing in case of different interactions the second channel starts to open up for higher gate voltages as the second channel in case of equal interactions.

In Figure 5.7b the local density as a function of site number j is presented. Firstly, the local density of the first and second subband is depicted for a gate voltage, such that only the first channel is open. Friedel oscillations are observed and in the central region the density of the first subband is nonzero, while the local density of the second band vanishes. Secondly, the evolution of the density with magnetic field is illustrated and it is noticed, that a nonzero magnetic field does not change the total density.

Magnetization indicates the difference between the local density of spin up and spin down, calculated as defined in eq. (4.42). Thus, it is zero in the absence of a magnetic field and increases with increasing magnetic field. It is studied for the first and the second subband for different gate voltages and in the case of equal and different interactions. In Figure 5.8 the magnetization as a function of the site number with equal interactions is depicted. In the first row for the first subband and in the second row for the second subband. Each for two different values of gate voltage, such that either only the first channel or both channels are open. If only the first channel is open (Fig. 5.8a), the magnetization of the first band has its maximal value in the central region, which increases with increasing magnetic field. For a particularly high magnetic field, the local magnetization at the central site becomes reduced. In the second subband the magnetization in the central site is zero, as expected and abruptly increases as the site number increases. This is enhanced with increasing magnetic field. In both subbands the envelope of the magnetization decays exponentially towards the outer region, while the magnetization oscillates due to the Friedel oscillations of the local density.

If both channels are open the magnetization of the first band has a maximum at the central

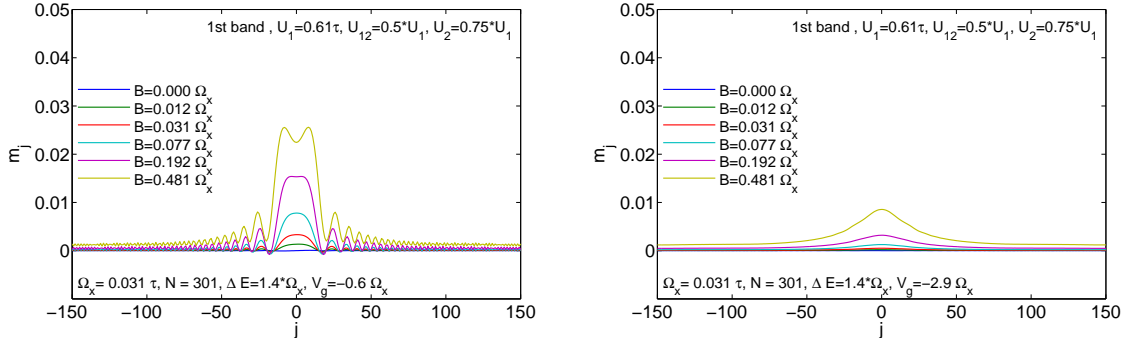
site and decays oscillating towards the outer flanks (Fig. 5.8b). The magnetization of the second subband is now maximal in the central region and rises with increasing magnetic field. Towards the outer region of the chain the magnetization shows the same oscillations and its envelope decays exponentially.

To understand the magnetization, one needs to picture the impact of a magnetic field on the effective potential and thus on the local density. A parallel magnetic field leads to an effective higher potential for the spin down electrons, while the spin up electrons experience an effective lower one, which does not affect the total local density for both spin types, but the spin-resolved local densities. The effective potential leads to a higher local density for spin up and to a lower local density for spin down as depicted in section 3.4 in Figure 3.7b. One can now understand that, if the local density is zero, the magnetic field has no impact, as e.g. in the central region of the unpopulated second band. With increasing site number the local density rises as well as the influence of the magnetic field. For small but finite local density its impact is especially high because it can yield such a high effective potential for spin down electrons that only spin up electrons can pass the constriction. This explains the maxima for the small site numbers, where the local density is nonzero, but small.

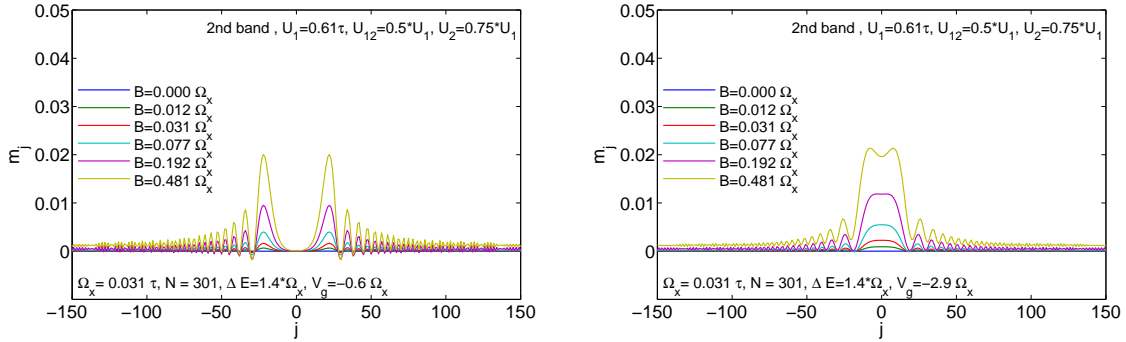
In Figure 5.9, for the sake of completeness, the four figures are shown in case of different interactions. The evolution is the same, as a well as each figure shows an equivalent situation.

The local susceptibility is computed via eq. (4.43) and depicted as a function of site number j in Figure 5.10. Susceptibility is the change of magnetization with magnetic field B and indicates the density of states at the Fermi level. The same four situations as in the magnetization are considered, i.e. susceptibility of the first and the second band for gate voltage such that either only the first band is populated or both are. Considering the susceptibility of the first band if only this one is populated (Fig. 5.10a), the expected maximum at the central site is observed, which is consistent with the observation in the magnetization of the first band at this value of gate voltage. The height of the maximum rises with the magnitude of interaction, i.e. the density of states at the chemical potential enhances. In Figure 5.10b where both bands are populated, we see that the impact of the increasing interaction on the susceptibility of the first band is weak, because the density of states at the chemical potential is very low. Considering the susceptibility of the second band for gate voltage such that only the first band is populated, consistent with Fig. 5.8c one observes a maximum, where the magnetization has its maximum as well. In Figure 5.10d the susceptibility of the second band in the case of such a low gate voltage that both bands are populated is depicted. The susceptibility is maximal in the central region and enhanced with increasing magnetic field.

In Figure 5.12 the total susceptibility as a function of gate voltage for several values of interaction U_1 of the first and second subband in the cases of equal and different interactions are compared. The total susceptibility is the sum of the local susceptibility within the interaction region (eq.(4.44)). The position of its maximum indicates the gate voltage, where the peak of the local density of states passes the chemical potential. The total susceptibility increases with increasing interaction. The maximum of the second band is shifted with higher interactions towards lower gate voltages. With equal interactions this effect is even more enhanced. In the case of different interactions the maximum of the second band lies below the maximum of the first band for all values of interaction, due to the smaller interactions in the second band. If all interactions are equal the maxima have

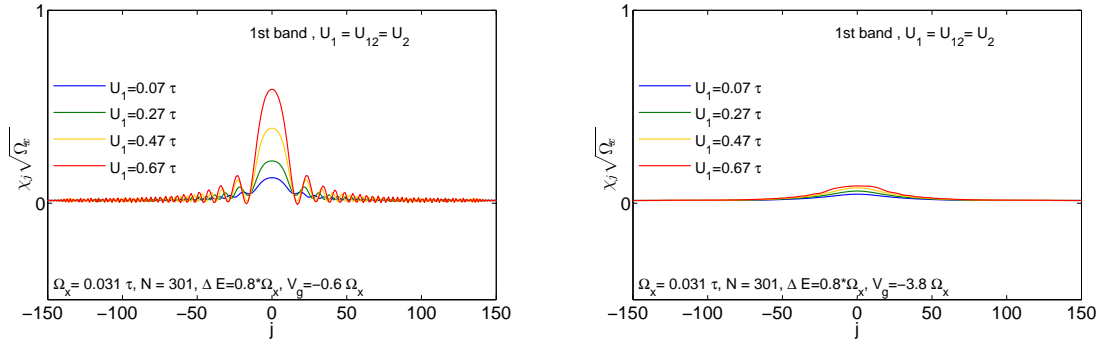


- (a) Local magnetization as a function of the site number j for the first subband. The gate voltage is chosen such that the first channel is open, while the second one is closed. The magnetization has its maximal value at the central region, which enhances with increasing magnetic field. With particular high magnetic field the effective potential for spin down electrons is too high, only spin up electrons can pass which leads to the small dip in the maximum.
- (b) Local magnetization as a function of the site number j for the first subband. The gate voltage is chosen such that both channels are open. Therefore, magnetization is rather small and has its maximum at the central site, which increases with increasing magnetic field.

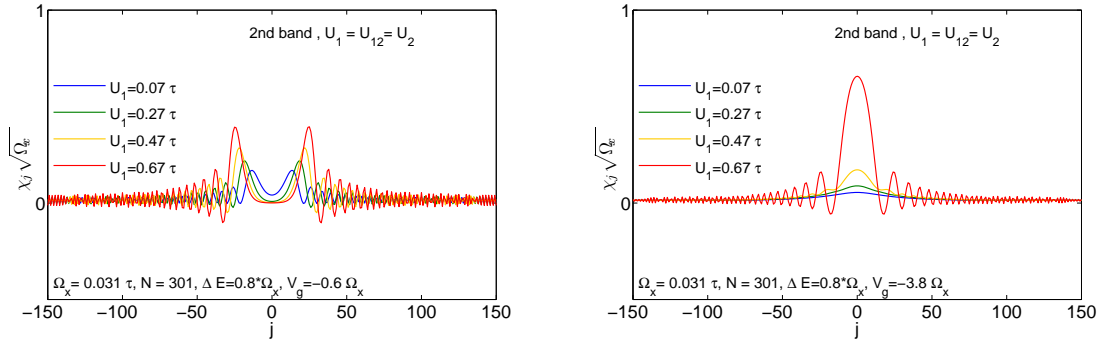


- (c) Local magnetization as a function of the site number j for the second subband. The gate voltage is chosen such that the first channel is open, while the second one is closed. Thus, in the central region there is no local density independent of the magnetic field. With decreasing potential towards the leads the density increases, because in this region the magnetic field not only lowers one spin resolved density while enhancing the other, but can lead to an effectively closed channel for spin down where spin up can already pass the constriction. With increasing magnetic field the magnetization rises.
- (d) Local magnetization as a function of the site number j for the second subband. The gate voltage is chosen such that both channels are open. Maximal magnetization is again observable in the central region, where for a very high magnetic field analogously as in Figure a) a dip arises in the maximum.

Figure 5.9.: The local magnetization as a function of the site number j for several values of the magnetic field B and different interactions. The upper row shows the magnetization in the first subband, the second row magnetization in the second subband. First column shows the magnetization for a gate voltage that leads to an open first, but closed second channel, while in the second column both channels are open. The different interactions do not change the behaviour of the magnetization compared to the case of equal interactions.



- (a) Local susceptibility as a function of the site number j for the first subband. The gate voltage is chosen such that the first channel is open, while the second one is closed. Maximum is in the central region and enhanced with rising interactions.
- (b) Local susceptibility as a function of the site number j for the first subband. The gate voltage is chosen such that both channels are open. Impact of the interaction is very weak, because the gate voltage is so low that independent of the interaction the spectral function at the chemical potential is very low.



- (c) Local susceptibility as a function of the site number j for the second subband. The gate voltage is chosen such that the first channel is open, while the second one is closed. Interaction enhances the shift of the maxima towards higher site numbers. The susceptibility is zero in the central region, since the potential lies above the chemical potential and thus the density of states is zero here. Maxima indicate where the peaks of the density of states lie at chemical potential.
- (d) Local susceptibility as a function of the site number j for the second subband. The gate voltage is chosen such that both channels are open. Maximal value of the susceptibility lies in the central region. Here the influence of the interaction on the sublevel spacing is very pronounced. In case of small interactions the susceptibility is very low because the gate voltage is so low that the potential of the second band lies much below the chemical potential. Differently for strong interactions, the susceptibility is high, here the peak of the density of states in the central region lies at the chemical potential.

Figure 5.10.: The local susceptibility as a function of the site number j for several values of the magnetic field B and equal interactions. The upper row shows the susceptibility in the first subband, the second row susceptibility in the second subband. First column shows the susceptibility for a gate voltage that leads to an open first, but closed second channel, while in the second row both channels are open.

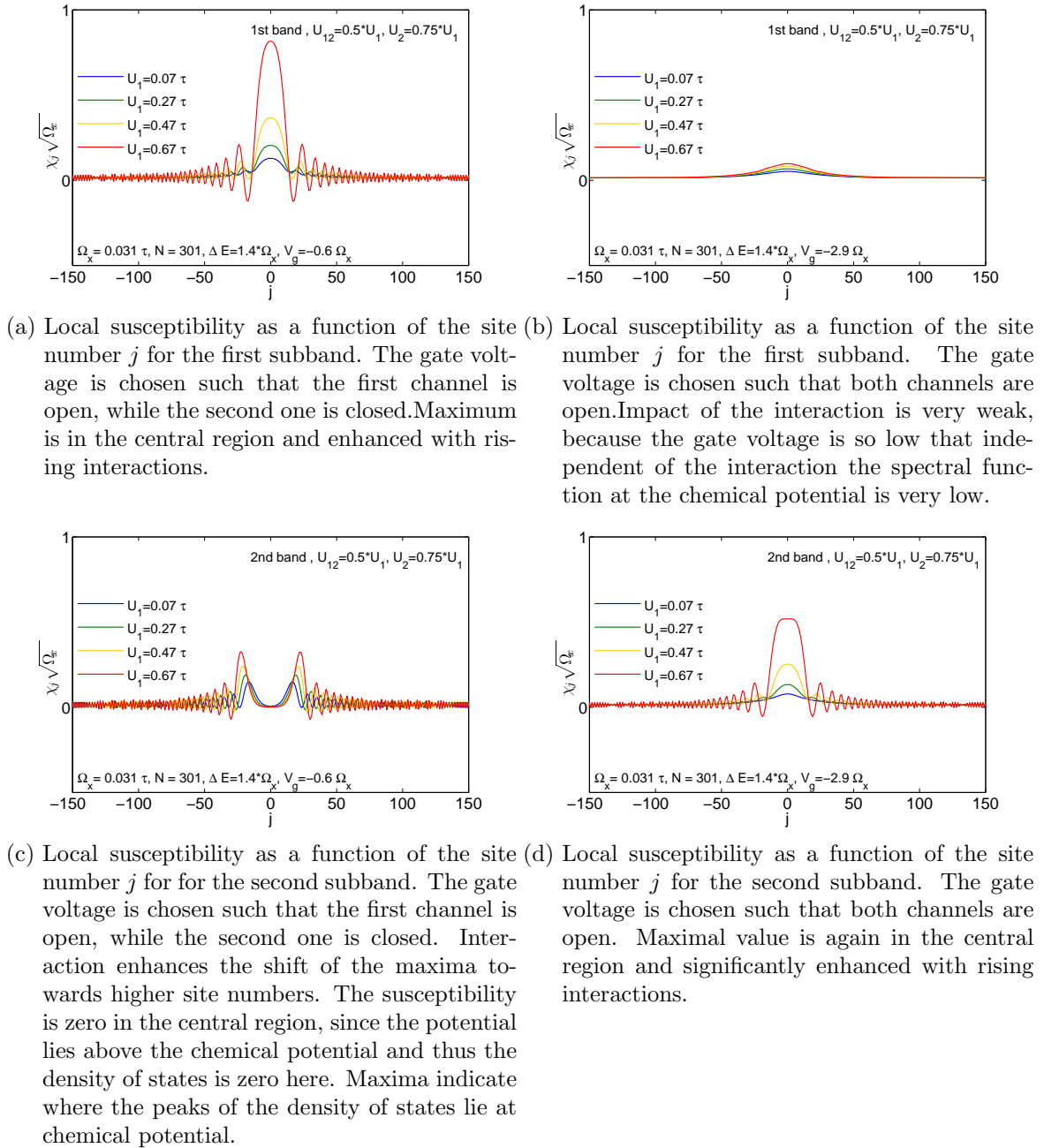
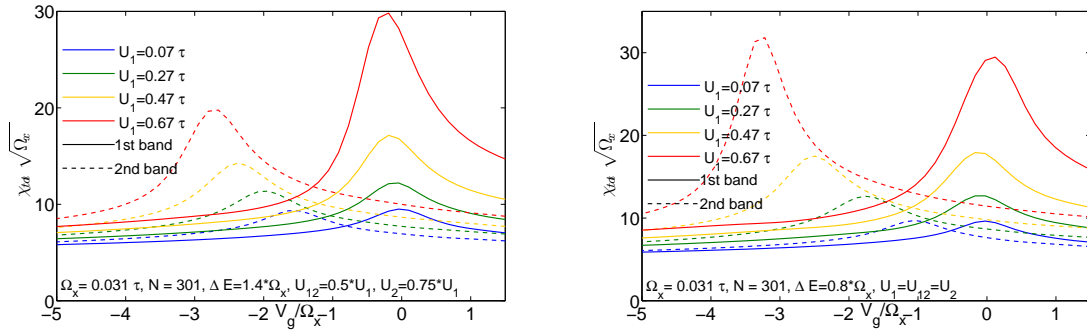


Figure 5.11.: The local susceptibility as a function of the site number j for several values of the magnetic field B and different interactions. The upper row shows the susceptibility in the first subband, the second row susceptibility in the second subband. First column shows the susceptibility for a gate voltage that leads to an open first, but closed second channel, while in the second row both channels are open. The different interactions do not change the behaviour of the magnetization compared to the case of equal interactions.



- (a) Total susceptibility as a function of gate voltage in case of different interactions. The maximal value of the susceptibility rises for the first and the second band with increasing interaction. It indicates the gate voltage, where the peak of the density of states in the central region passes the chemical potential. The maximal value of the second band is shifted with increasing interaction towards lower gate voltage and lies below the maximum of the first band, due to the smaller interaction in the second band.
- (b) Total susceptibility as a function of gate voltage in case of equal interactions. The position of the maximum indicates the gate voltage where the peak of the density of states passes the chemical value. The maximal value increases with increasing interaction. The maximum of the second band is shifted much more towards lower gate voltage with increasing interaction as in case of different interactions. Its maximal value equals the maximal value of the first band, except for the highest value of interaction, where it even lies above the maximum of the first band.

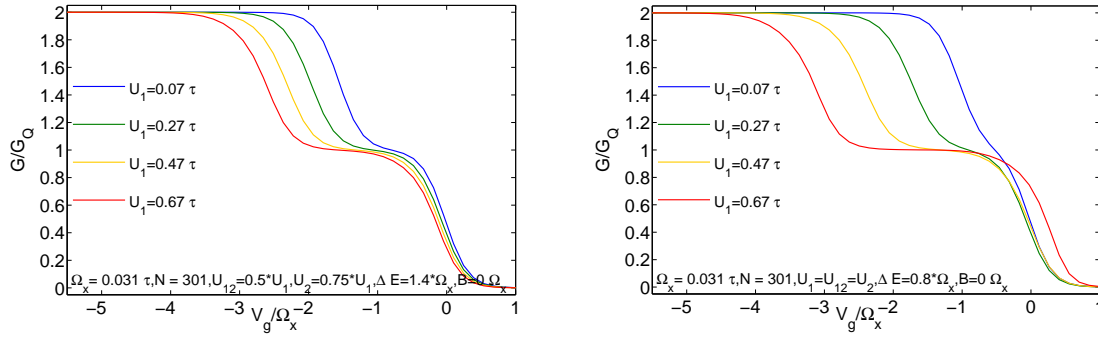
Figure 5.12.: Total susceptibility for different and equal interactions as a function of gate voltage.

equal values, with very high interaction the susceptibility of the second band shows even a higher maximum.

Finally, the conductance as a function of gate voltage for several values of interaction is investigated. Although this is not an experimental measurable quantity, it is important to investigate the impact of the magnitude of the interaction. Its impact on the conductance of the first channel is very different between the two possibilities of interaction. In the case of different interaction (Fig. 5.13a) both conductance steps show a more pronounced shoulder and shifted towards lower gate voltage with increasing interaction. This effect is largely enhanced in the second step by the high local density of the first subband, such that the width of the first plateau increases with increasing interaction.

If the interactions are chosen to be equal, the impact of the interaction changes in the first step. For small but increasing interaction the step also becomes shifted, but higher increasing interactions lead to contrary behaviour. The increase leads to a big shift towards higher gate voltages. In the second step the evolution with increasing interaction leads again to a more pronounced shoulder and a shifted step and the impact is also much bigger as in the first step due to the filled first subband and even larger than in the case of different interactions.

We can conclude that we observe with our model a second conductance step, where the choice of interaction is very important. It defines the effective sublevel spacing as well as the response of the conductance to the magnetic field. The response of the magnetic field in the first step is as expected (Fig. 5.5a and 5.5d). The response of the second step is respectively



- (a) Conductance as a function of gate voltage for several values of interaction for a two-band model with different interactions. With increasing interaction the steps show a more pronounced shoulder and become shifted towards lower gate voltages. This effect is largely enhanced in the second step by the high local density of the first channel.
- (b) Conductance as a function of gate voltage for several values of interaction for a two-band model with equal interactions. Small, but increasing interactions lead to a more pronounced shoulder and a shifted step in direction of smaller gate voltage, while high interaction yield the inverse behaviour and shift the first step in opposite direction. Differently the second step is shifted significantly towards smaller gate voltage with increasing interaction, which is amplified by the high local density of the first channel.

Figure 5.13.: Conductance plotted as a function of gate voltage for several values of the interaction U_1 . In the left plot the interactions are chosen differently, while in the right plot all interactions are equal. This leads to very different behaviour in the first step.

smaller or equal, depending on the choice of interaction. Comparing it with measurements as depicted in Figure 3.3b, the computed second step shows different behaviour. While the measurement shows a shift with increasing magnetic field, the computed second conductance step is fanned out in the lower part around a center point, where all conductance curves intersect.

Moreover, we can state that the local density of the first mode is affected by the density of the second one as expected and observations in the magnetization and local and total susceptibility are in agreement with the results of Bauer et al. [4] such as high magnetization and an accordingly high susceptibility in the central region of an open transport channel.

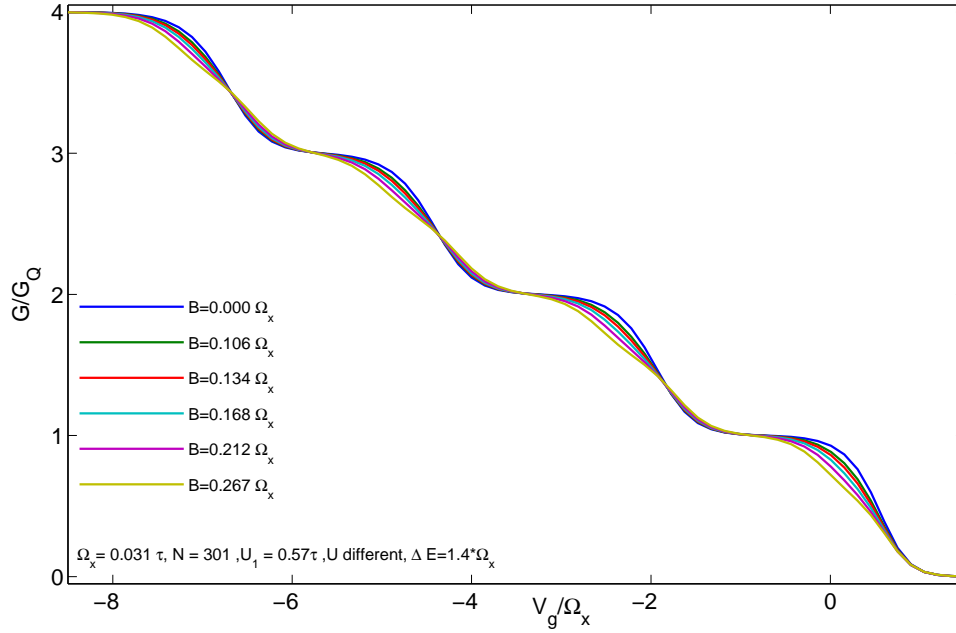


Figure 5.14.: Conductance plotted as a function of gate voltage for a four-band model with different interactions. With increasing magnetic field the steps show a more pronounced shoulder. But differently to the observation in the one or two-band model, the highest magnetic field does not yet yield the expected spin-resolved plateaus, but only a smaller slope. The change in the conductance with increasing magnetic field decreases towards higher steps. The most pronounced difference between the first and the higher steps is the fanned out lower part of the higher steps which is not observed in the first step.

5.3. QPC modelled with four subbands

The quantum point contact is now studied with four subbands. As in the previous section we will consider two different cases of interaction. The first case is to choose all interactions equal. The second one is to calculate them via eq. (4.6), such that

$$\begin{aligned}
 U_{12} &= 0.5 \cdot U_1 & U_{13} &= 0.375 \cdot U_1 & U_{14} &= 0.3125 \cdot U_1 \\
 U_{22} &= 0.75 \cdot U_1 & U_{23} &= 0.4375 \cdot U_1 & U_{24} &= 0.344 \cdot U_1 \\
 U_{33} &= 0.64 \cdot U_1 & U_{34} &= 0.398 \cdot U_1 & U_{44} &= 0.57 \cdot U_1
 \end{aligned} \tag{5.3}$$

This choice of interaction we will again label as 'different interactions'. The sublevel spacings are chosen equally between the different transversal modes to observe the effect of the interactions on it.

The computed conductance with different interaction is considered in Figure 5.14 as function of gate voltage. Magnetic field leads in all four steps to the same effect, a smaller slope. In all other conductance steps except the first one, it yields a fanned out step in the lower part. In the four-band model even the biggest magnetic field does not show an approach towards spin-resolved plateaus. Obviously, the effect of the magnetic field is smaller compared to effect of the same field in a two-band model.

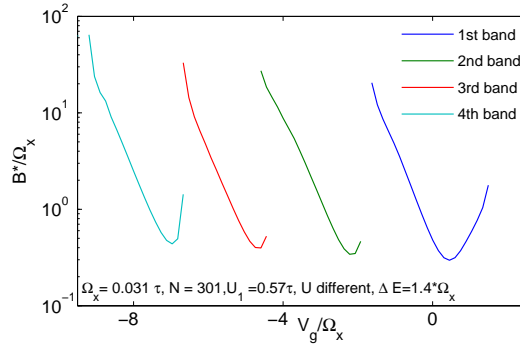
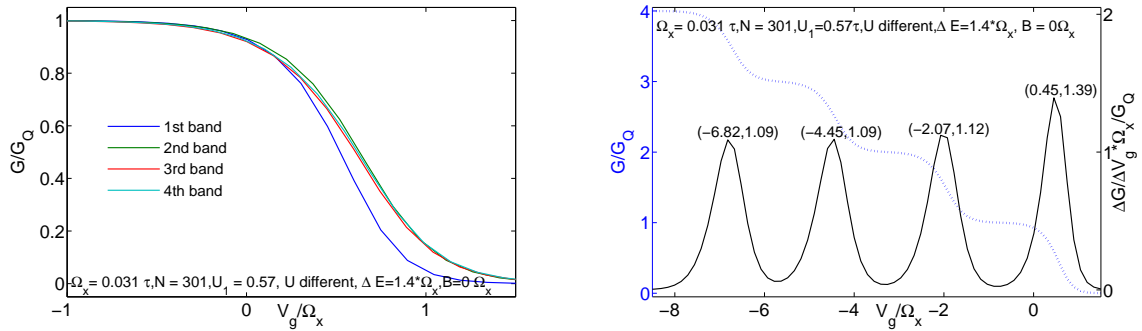


Figure 5.15.: Low-energy scale B^* plotted logarithmically as a function of gate voltage for the four subbands. It can be observed that minimum of B^* rises with number of the subband, i.e. for higher conductance step the influence of the magnetic field decreases.

The impact of the magnetic field decreases with increasing number of subband. This is confirmed, if one considers the low-energy scale B^* (Fig. 5.15). B^* again depends exponentially on $-V_g$. Looking at the minima, it is noticeable that they increase with increasing subband number, i.e. the influence decreases.

Since one is interested in the different behaviour of the conductance through each band, in Figure 5.16a the four steps are plotted individually and shifted towards the first step to compare them. One can see that the second, third and fourth step show nearly the same slope, while the slope of the first conductance step is larger.

This is confirmed in Figure 5.16b, where the conductance with $B = 0 \Omega_x$ and its derivative with respect to gate voltage is depicted. Here it is noticed as well that the first slope is



(a) Comparison of conductance steps for the four-band model. Second, third and fourth conductance step are shifted artificially to be able to compare them. It is noticeable that the first step has a very different rise compared to the other three.

(b) Derivative of the conductance with different interactions with respect to the gate voltage. The width of the conductance steps can be read off the position of the maxima of the conductance. One can see that the first plateau is broader, while the other are equidistant. Further, a higher slope is observed in the first step compared to the successive ones.

Figure 5.16.: Comparison of the conductance steps and the derivative of the conductance in a four-band model with different interactions.

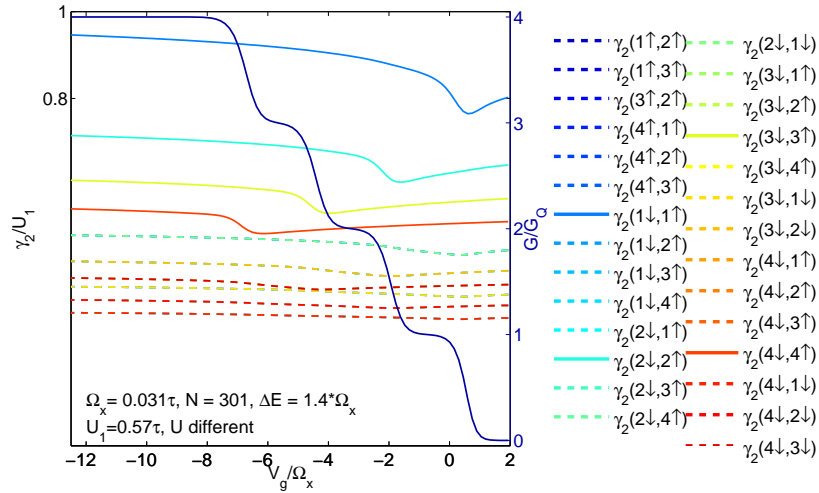


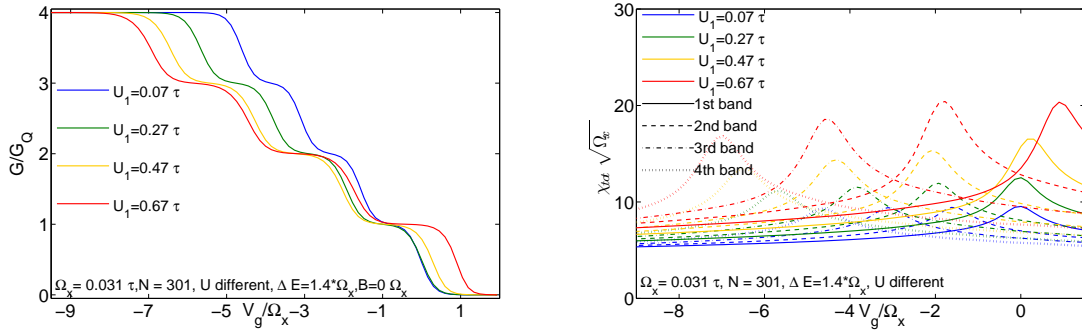
Figure 5.17.: Conductance and vertex function at the central site plotted as a function of gate voltage for a four-band model in the case of different interactions. The vertex functions decrease with increasing number of the involved subbands, as well as interaction between different subbands is smaller. All vertex function show a minimum, when the respective conductance step starts to rise.

larger than the slope of the higher steps. As it can be read off from the positions of the maxima of the derivative, the three higher steps are nearly equidistant, only the first step is slightly broader.

In Figure 5.17 the vertex function at the central site and the according conductance with $B = 0\Omega_x$ are depicted as a function of gate voltage. The vertex functions are measured in units of the initial value of the first chain U_1 . The interactions are initialized as different, i.e. the interaction decreases with increasing number of the involved subbands, as well as interactions between subbands are smaller as on one chain. Hence, it is expected that the largest vertex function is $\gamma_2(1\uparrow, 1\downarrow)$ and the other vertex function are accordingly smaller. Those vertex functions that are effective interactions on the same subband are depicted by solid lines. Each of these vertex functions has a minimum in the regime of gate voltage, where the respective transport channel opens. Vertex functions between different subbands are illustrated with dashed lines and show only small or no minima. None of the vertex functions become considerably larger than their initial value.

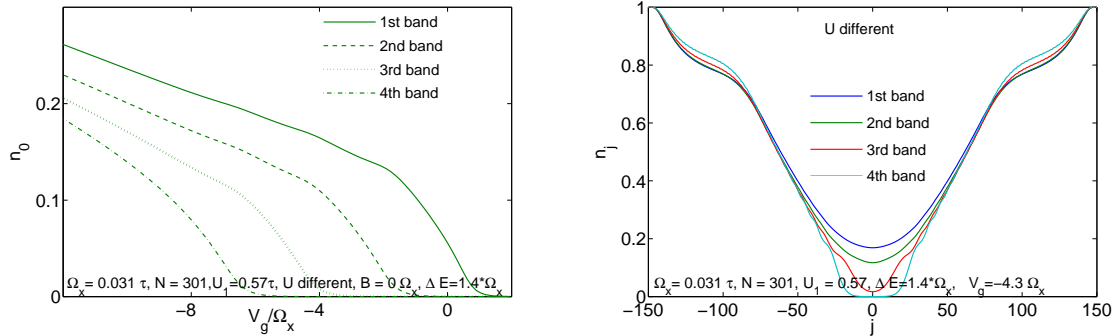
In Figure 5.18a conductance as a function of gate voltage for several values of interaction is depicted. For small interaction the increase leads to a shift towards smaller gate voltage. But for high interactions this behaviour becomes inverse and the conductance is shifted towards higher gate voltage. With increasing interaction the width of the plateaus enhances. This effect is even stronger in higher modes due to the amplifying effect of the local density of the lower subbands. It appears to be smaller for high interaction, but this is due to the overall shift of the conductance graph.

The total susceptibility as a function of gate voltage for the four subbands in case of different interactions is illustrated in Figure 5.18b. The maxima indicate the gate voltage, where the peak of density of states of the respective subband passes the chemical potential. Consistent with Figure 5.18a the maxima of the first band are shifted towards higher gate voltage. The



- (a) Conductance plotted as a function of gate voltage for a four-band model for several values of the interaction in case of different interactions. Increasing interactions lead to a shift towards smaller gate voltages and a more pronounced shoulder. Very high interaction leads to inverse behaviour and a pronounced shift towards higher gate voltage of the whole graph. The plateau widths are enhanced by higher interactions, even more for the higher steps due to the amplifying effect of the local density of the lower subbands.
- (b) Total susceptibility as a function of gate voltage for the four subbands in case of different interactions. Maxima of the total susceptibility of the four subbands indicate the gate voltage, where the corresponding peak of the density of states passes the chemical potential. Consistent with Fig. 5.18a the maxima of the first band are shifted towards higher gate voltage. The stronger the interactions the larger is the shift. Due to the increasing width of the plateaus with increasing interactions, the maxima of the fourth band are pushed accordingly towards lower gate voltages. The intervals between the maxima of the four subbands are nearly identical for one choice of interaction

Figure 5.18.: Conductance and total susceptibility as a function of gate voltage for several value of interaction U_1 .



- (a) Local density plotted as a function of gate voltage in case of different interactions. The influence of the subband on each other is very pronounced. When the local density of a subsequent subband starts to rise, it yields a kink in the local density of the subband prior to it.
- (b) Local density plotted as a function of site number in case of different interactions. The influence of the subband on each other is pronounced as well. The local density of each successive band lowers the slope of the density of previous band. In particular, the influence of the third on the fourth subband is apparent.

Figure 5.19.: Local density in case of different interactions

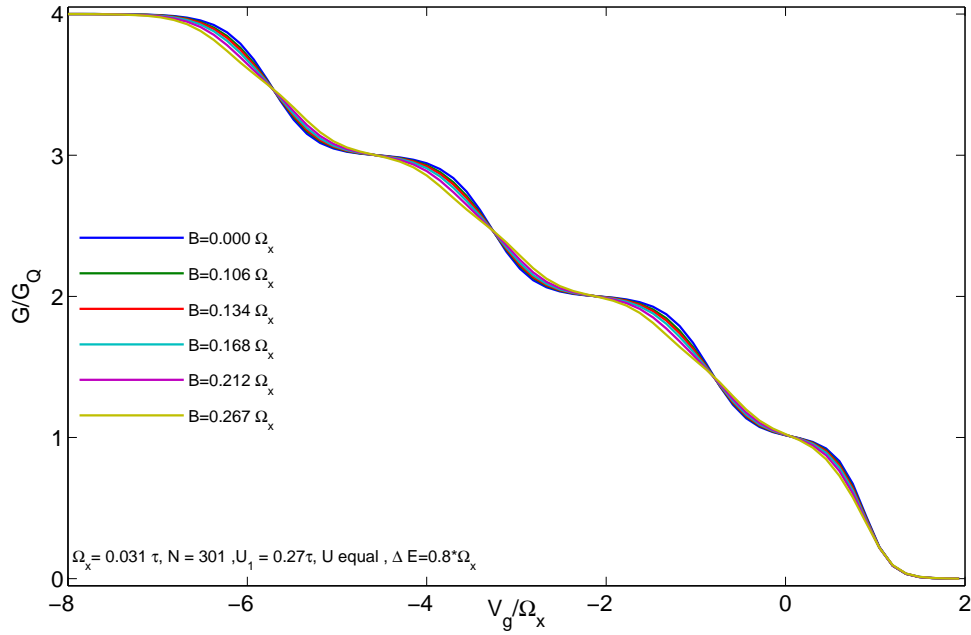
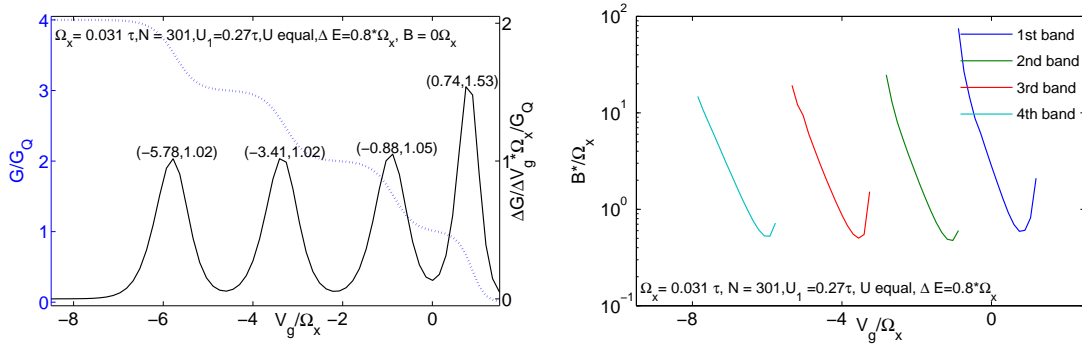


Figure 5.20.: Conductance plotted as a function of gate voltage for a four-band model with equal interactions. It is conspicuous that the first conductance steps starts to rise already at a gate voltage much higher than zero. The influence of the magnetic field is small, especially in the first step due to the small interaction. It can be observed that the first step has a larger slope than the other steps.

stronger the interactions the larger is the shift. Due to the increasing width of the plateaus with increasing interactions, the maxima of the fourth band are pushed accordingly towards lower gate voltages. The intervals between the maxima of the four subbands are nearly identical for one choice of interaction.

The local density of the several bands affect each other explicitly, as observable in Figure 5.19. In Figure 5.19a the local density at the central site is depicted as a function of gate voltage. If the local density of the second subband rises, this yields a pronounced kink in the local density of the first band. Equally this happens in all further bands, i.e. if the local density of a band starts to rise it yields a strong kink in the band prior to it. An effect of the higher subbands (e.g. the third or fourth) on the local density of the first band is not observable explicitly. Considering the local density as a function of site number an equal, pronounced impact of the successive subbands on each other is observed (Fig. 5.19b). In particular, the influence of the third on the fourth subband is apparent.

Now, the case of equal interactions is considered. In Figure 5.20 the conductance is depicted as a function of gate voltage. The depicted plot is computed with a small interactions compared to e.g. the respective plot in case of different interactions. This is due to the fact that the choice of equal interactions yields to divergencies at much smaller interactions, i.e. already with $U_1 = 0.57\tau$ the vertex functions diverge. Further it can be noticed that the whole graph is shifted towards higher gate voltages, where the first channel in this case already opens up at around $V_g \approx 1 \Omega_x$. This is a first hint of the unphysical behaviour, which



- (a) Derivative of the conductance with respect to the gate voltage. The width of the conductance plateaus can be read off the position of the maxima of the conductance. One can see that the first plateau is clearly shorter, while the other are equidistant. The derivative of the first conductance step is considerably higher as of the other steps.
- (b) Low-energy scale B^* plotted logarithmically as a function of gate voltage for the four subbands. It can be observed that the minima of B^* are equal for all subbands except the first one. The minimum of the first subband is even slightly higher, i.e. the influence of the magnetic field is smaller.

Figure 5.21.: Derivative of the conductance and low-energy scale B^* in case of equal interactions

we observe for this choice of interactions in a four-band model. This shift enhances strongly with increasing interactions as we will see below.

For this rather small interaction, we can see that the first step changes very little with increasing magnetic field, while the change in the higher step is analogous to the change as observed above in case of different interactions. The slope decreases, but the magnetic field is not yet high enough to yield the spin-resolved plateaus in this model.

The influence of the magnetic field can also be read off the low-energy scale B^* as depicted in Figure 5.21b. B^* again depends exponentially on $-V_g$. The minima of B^* are at the same height in all bands except the first band, which has a minimum with a larger value, which confirms that the influence on the first step is smaller. Taking the derivative of the conductance with respect to the gate voltage makes the width of the plateaus observable. The conductance with $B = 0 \Omega_x$ and its corresponding derivative is illustrated in Figure 5.21a. The first step is shorter as the successive ones, which are equidistant and explicitly larger. Furthermore, the first derivative is larger, i.e. the rise of the first step is bigger.

In Figure 5.22 conductance with $B = 0 \Omega_x$ and the corresponding the vertex functions at the central site are depicted as a function of gate voltage. The vertex functions are measured in units of the initial value U_1 and all initial interactions are equal. It can be observed that the vertex functions are a little bit smaller as their initial value and only differ very little within the considered regime of gate voltage. In the regime of gate voltage, where the first conductance step rises, the vertex function $\gamma_2(1 \uparrow, 1 \downarrow)$ has its minimum, while the dominant one is the vertex function $\gamma_2(4 \uparrow, 4 \downarrow)$. The minima of the several vertex function move towards smaller gate voltage with higher number of the involved subbands, such that the minima are located at the gate voltage, where the respective conductance starts to rise.

The local density of the four subbands is depicted in Figure 5.23. In Figure 5.23a local density of the central site is illustrated as a function of gate voltage. Here, equal behaviour

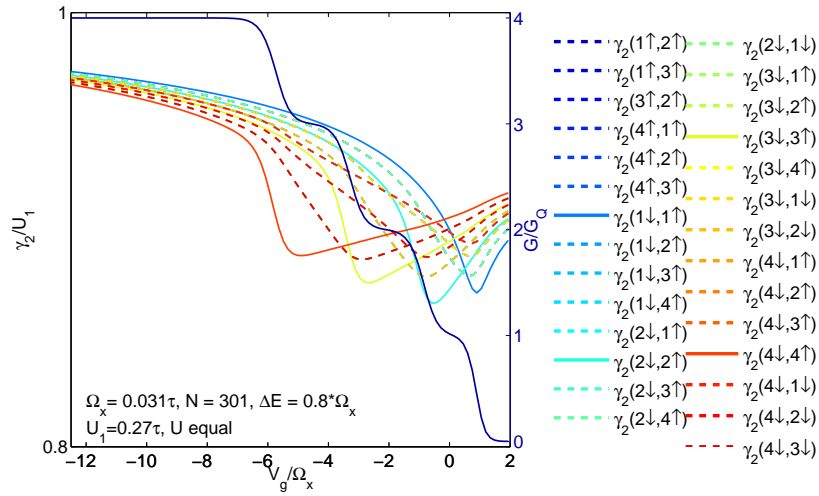
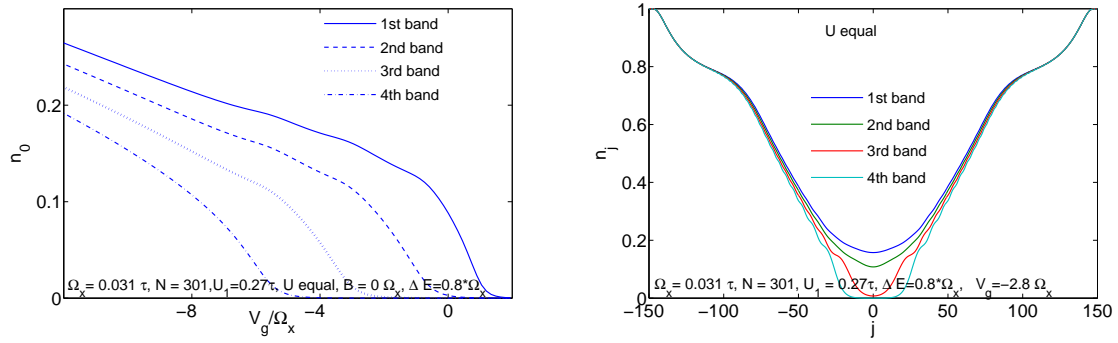


Figure 5.22.: Conductance and vertex function at the central site plotted as a function of gate voltage for a four-band model in the case of equal interactions. It can be observed that the vertex functions become smaller than their initial value. The minima of the several vertex function move towards smaller gate voltage with higher number of the involved subbands, such that the minima are located at the gate voltage, where the respective conductance starts to rise. The overall change is not very pronounced, no strong screening effects can be observed. In the regime of gate voltage, where the first channel opens up, $\gamma_2(1 \uparrow, 1 \downarrow)$ has its minimum, while $\gamma_2(4 \uparrow, 4 \downarrow)$ dominates.



(a) Local density plotted as a function of gate voltage in case of equal interactions. The influence of the subbands on each other is very pronounced. When the local density of a subsequent subband starts to rise, it yields a kink in the local density of the subband prior to it.

(b) Local density plotted as a function of site number in case of equal interactions. Again the influence of the subbands on each other is very pronounced. It can be observed that each slope is influenced by the local density of the successive bands.

Figure 5.23.: Local density in case of equal interactions

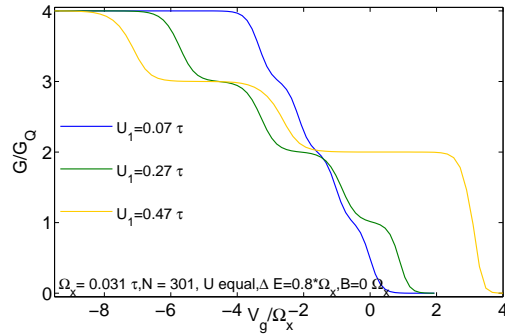
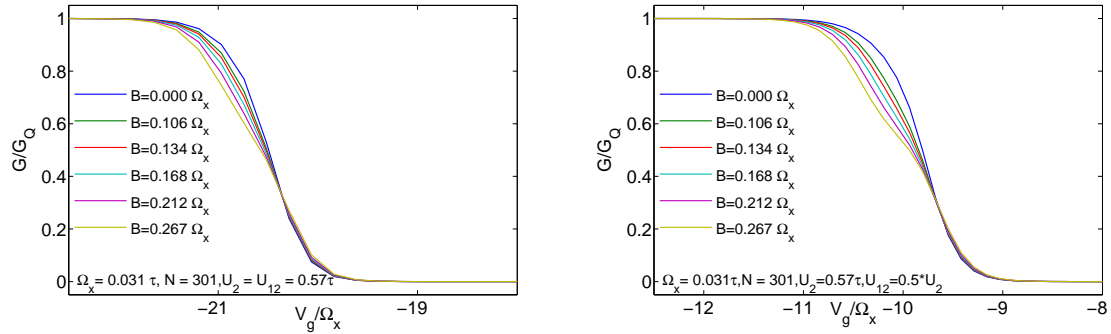


Figure 5.24.: Conductance plotted as a function of gate voltage for a four-band model for several values of the interaction in the case of equal interactions. With higher interaction the behaviour becomes unphysical: The effective potential is so low, that the first channel opens up at gate voltages much higher than zero and a plateau at $G = G_Q$ is not observable.

can be observed as in the case of different interactions: The rise of the local density of each subsequent channel yields a kink in the rising density of the band prior to it, while the third or fourth band does not affect the local density of the first band explicitly. Local density as a function of site number shows as well a pronounced impact of the successive bands on the local density of each band (Fig. 5.23b).

In Figure 5.24 it is illustrated, how higher interactions effect the conductance. Conductance in case of zero magnetic field as a function of gate voltage is depicted. For an interaction $U_1 = 0.47$ the effective potential is so low that the conductance becomes nonzero already for a gate voltage much higher than zero. Furthermore, the first two steps become indistinguishable, there is no plateau at $G = 1G_Q$ visible. Thus, the choice of equal interaction leads to unphysical behaviour in the conductance

We can conclude that the choice of interactions in a four-band model strongly influences the conductance. If the interactions are all chosen equal, the effective potential is so low that the transport channels open up at very high gate voltage, which is in no agreement with experimental observations. This effect is already observable with small interactions, but largely enhanced with increasing interactions. A better choice seems to be the different interactions, chosen as defined in eq. (5.3). In this case the observation are in better agreement with experiments. We observe that the first step always behaves differently to the higher ones with a higher slope and a greater response to a magnetic field. But the response of the higher conductance step on the magnetic field is different compared to the experiments, as depicted in Figure 3.3b. While in the experiment an increasing magnetic field shifts the higher conductance steps, we rather observe that the steps fan out in the lower part of the step. Moreover, a pronounced influence of the higher modes on the conductance is noticed. Although the local density within the central region of the higher modes is zero, in the regime, where the first transport channel opens, the density in the boundaries of the constriction region apparently affects the potential and therefore the first conductance step.



- (a) Conductance of the second band plotted as a function of gate voltage for several values of magnetic field in case of equal interactions. The high local density of the lower band yields such a high effective potential that the conductance does not start to rise until $V_g \approx -20 \Omega_x$. Compared to the case of different interactions the influence of the magnetic field is depleted.
- (b) Conductance of the second band plotted as a function of gate voltage for several values of magnetic field in case of different interactions. The high local density of the lower band yields such a high effective potential that the conductance does not start to rise until $V_g \approx -9.5 \Omega_x$. The influence of the magnetic field is higher as in the case of equal interactions.

Figure 5.25.: Conductance of the second band as a function of gate voltage with a half-filled first subband.

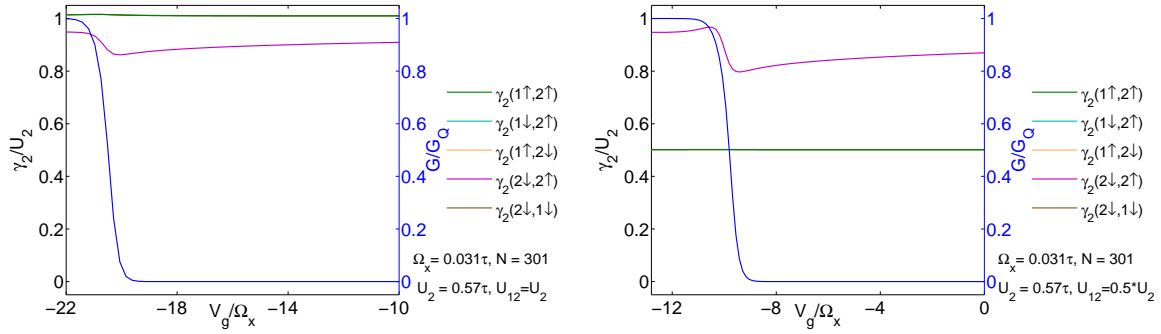
5.4. Effect of one half-filled subband on the conductance

The final considered system consists of two bands, where the lower one is half-filled. Only conductance through the second band is computed under the influence of the lower band. Interactions in the lower band are turned off, i.e. $U_1 = 0$, interactions between the bands are nonzero ($U_{12} \neq 0$). This way the influence of a half-filled band is investigated, which models the impact of a nearly constant background. Recalling the dispersion relation of a tight-binding chain (Fig. 3.4a), it becomes apparent that if the lower chain is initialized in particle-hole symmetry, a change in energy only slightly affects the density of states and thus the local density. An example of such a constant background in an experiment would be the metal gates within the quantum point contact.

In Figure 5.25 conductance of the second band is depicted as a function of gate voltage. The high local density of the first band yields such a high effective potential that the conductance of the second band does not start to rise until $V_g \approx -20 \Omega_x$ in case of equal interactions and $V_g \approx -9.5 \Omega_x$ in case of different interactions. Surprisingly, the effect of the magnetic field is in case of different interactions higher than in case of equal interactions.

Considering the local density of the first and second subband in case of gate voltages, where the conductance is about to become nonzero, one observes the known shape of the local density in the second band (Fig. 5.27). In the first band the local density is very high with a maximum in the central region of $n_0 = 1.18$ in case of equal interactions and $n_0 = 1.09$ in case of different interactions.

The vertex functions in case of equal interactions are accordingly high (Fig. 5.26a), where it is not surprising that the vertex functions $\gamma_2(1\sigma, 2\sigma')$ are bigger than $\gamma_2(2\uparrow, 2\downarrow)$. While the first one does not change at all over whole regime of gate voltage, $\gamma_2(2\uparrow, 2\downarrow)$ shows



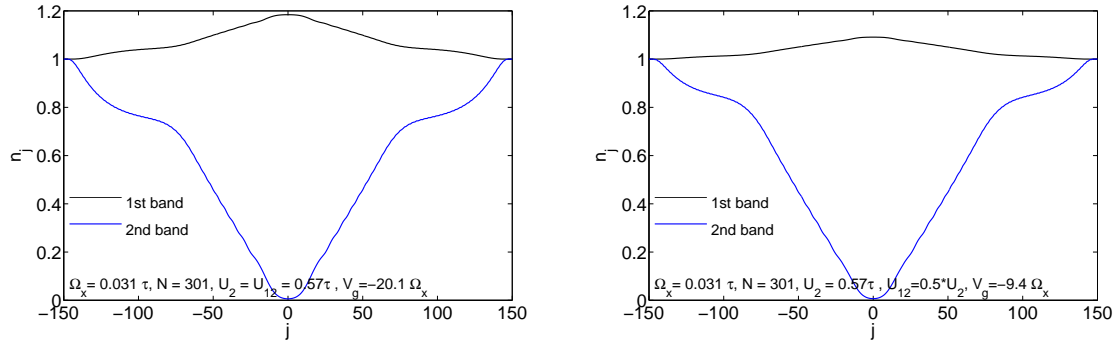
- (a) In the case of equal interactions the dominant vertex functions are $\gamma_2(1\sigma, 2\sigma')$, which stay at its initial value at all time. The vertex function $\gamma_2(2\uparrow, 2\downarrow)$ is smaller and also smaller as its initial value.
- (b) In the case of different interactions, where the interaction between the bands is half the value of the onchain interaction in the second band, the vertex function $\gamma_2(2\uparrow, 2\downarrow)$ is larger and has a maximum, where the conductance bends. It is slightly smaller as its initial value. The vertex functions $\gamma_2(1\sigma, 2\sigma')$ are smaller and stay constant over the whole regime of gate voltage.

Figure 5.26.: Conductance and vertex function at the central site of the second subband as a function of gate voltage with a half-filled first subband.

again a minimum, when the conductance starts to rise. The vertex function behaves similar in case of different interactions (Fig. 5.26b), where the only difference is that $\gamma_2(1\sigma, 2\sigma')$ is accordingly at half the value. Further the minimum of $\gamma_2(2\uparrow, 2\downarrow)$ is more pronounced in this case.

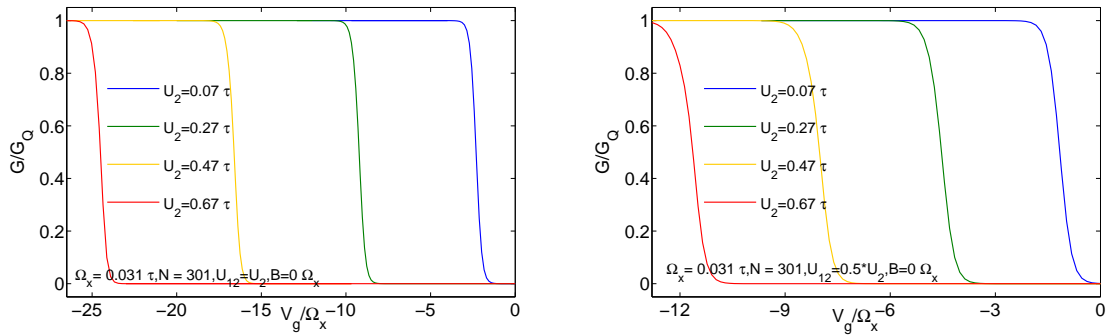
With increasing interaction the impact of the high local density of the first band is enhanced, i.e. the conductance rises for lower gate voltage the stronger the interactions are (see Fig. 5.28). In case of equal interaction the impact is even larger.

Thus, we can conclude that a constant background of high local density increases the effective potential severely, and thus leads to a constant shift towards lower gate voltage according to the interactions, but does not affect the vertex function nor the form of the conductance in particular.



- (a) As observable in the conductance the high local density in the first subband yields a high effective potential, thus that the local density in the central region starts to rise for $V_g = -20.1 \Omega_x$. In case of equal interactions the local density in the first subband in the central region at this gate voltage around $n_0 = 1.18$, i.e. is very high.
- (b) As observable in the conductance the high local density in the first subband yields a high effective potential, thus that the local density in the central region starts to rise for $V_g = -9.4 \Omega_x$. In case of different interactions the local density in the first subband in the central region at this gate voltage around $n_0 = 1.09$ and thus is not as high as in the equal case but still large.

Figure 5.27.: Local density of the first and second subband in case of an initial half-filled first subband for equal and different interactions.



- (a) Conductance of the first band under the influence of a half-filled subband for equal interactions. With increasing interactions the conductance step is shifted more and more towards smaller gate voltage. In case of equal interactions the shift is even larger compared to different interactions.
- (b) Conductance of the first band under the influence of a half-filled subband for different interactions. With increasing interactions the conductance step is shifted more and more towards smaller gate voltage.

Figure 5.28.: Comparison of the conductance of the second band under the influence of a half-filled subband for equal and different interactions

6. Conclusion and Outlook

The origin of the 0.7 anomaly of a quantum point contact is subject of investigation and discussions for nearly 20 years. Bauer et al. [4] recently found a consistent explanation of this phenomenon and its numerous related observations.

The present thesis is motivated by their work and presents a model, that offers the possibility to observe conductance through a quantum point contact with more than one transport channel. A model with n chains is used, where on-site interaction on one chain and in between the chains is assumed, while interband transitions are neglected. Modelling a QPC with n subbands aims to explain why the 0.7 anomaly is typically significantly featured only in the first conductance step.

Within this model fRG equations have been derived and used to compute the full, renormalized Green's function of this system. This in turn is used to compute several observables, in particular the conductance.

Three different situations have been modeled: A QPC with two subbands and with four subbands as well as a model of two subbands, where the lower half-filled band affects the conductance of the second band. This way the impact of a background of a nearly constant local density of electrons is investigated. All considered systems have been studied with two choices of interactions. In the first case, all interactions are chosen to be equal. In the second case, a ratio of the interactions has been computed via overlap integrals between the wave functions within a quadratic potential.

We computed up to four conductance steps with our model and show that the conductance of the first mode behaves differently compared to the higher ones. The first step shows a higher slope and a different response to the magnetic field. Moreover, the first conductance step seems to be affected by the higher modes. In addition to the expected impact of the local density of higher modes on the density of the first mode, when the concerning channels open up, the density in the boundaries seems to affect the local potential and hence the first conductance step. Magnetization as well as local and total susceptibility, considered within the two-band model, are in agreement with the results of Bauer. For an open channel a high magnetization and susceptibility in the central region of the constriction are observed. The effect of the magnetic field on the higher conductance step is not in perfect agreement with experiments and needs to be subject of further studies. The choice of interaction, in particular in the four-band model, is an important issue, since it strongly influences the results. Choosing the inter- and intraband interactions to be equal can yield unphysical behaviour and convergence problems for high interactions, while choosing the interactions as different leads to better results. The model with a half-filled subband shows that a background of high local density yields a high effective potential, i.e. a conductance step that rises at very low gate voltage, but does not change the physics.

An important future concern should be a systematic analysis of the strong influence of the choice of interactions and the impact of higher modes on the first conductance step.

A. Transport through coupled quantum wires

As some preliminary studies a system of two parallel, coupled quantum wires has been considered within the static fRG 1 scheme with nearest neighbour interactions. In the fRG 1 scheme only the first fRG equation (2.19) is taken into account and the full interaction is substituted by the bare interaction, i.e. the vertex flow is neglected, see section 2.4. In two different models the conductance is computed with and without interactions to compare the results. The models are motivated by Atland et al. [22] and Nakaharai et al. [23]. The noninteracting system can be explained in a single-particle-picture and it will be shown that interactions renormalize the interchain hopping and velocity of the electron, but we find no indication that they change the system's behavior in a fundamental manner.

A.1. Models

A.1.1. Model I

The first model describes two parallel chains, where electrons interact with each other on the chain and with electrons on the same site of the other chain within a scattering region. Both chains are finite on one site and coupled to a noninteracting lead on the other site. The model is depicted in Figure A.1.

We are working with a Hamiltonian of a spinless system, which can be separated in three parts:

$$H = H_u + H_d + H_{ud} \quad (\text{A.1})$$

Hamiltonian of the upper chain:

$$H_u = \sum_{i=-\infty}^N -\mu n_{i,u} + \tau(c_{i+1,u}^\dagger c_{i,u} + h.c.) + \sum_{i=-N+1}^N U n_{i,u} n_{i+1,u} \quad (\text{A.2})$$

Hamiltonian of the lower chain:

$$H_d = \sum_{i=1}^{\infty} -\mu n_{i,d} + \tau(c_{i+1,d}^\dagger c_{i,d} + h.c.) + \sum_{i=1}^{N+N_1} U n_{i,d} n_{i+1,d} \quad (\text{A.3})$$

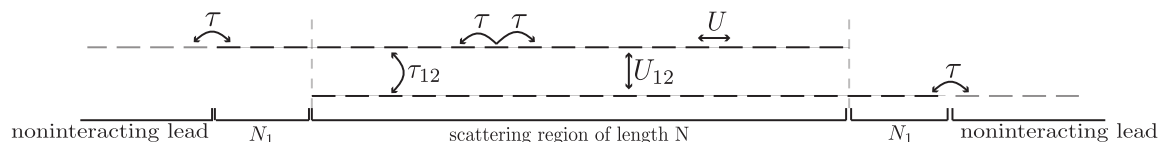


Figure A.1.: Model I with two leads

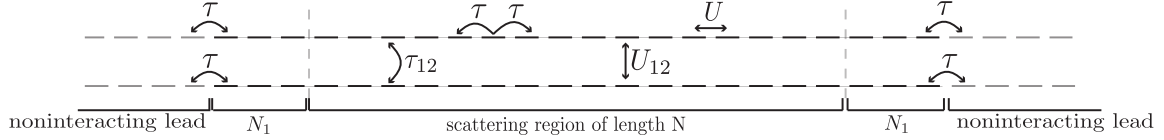


Figure A.2.: Model II without finite ends. This model is expected to show less boundary effects.

τ is the nearest-neighbour hopping amplitude, U is a nearest-neighbour interaction.

The third part describes hopping with τ_{12} as interchain hopping and interaction U_{12} in between the chains:

$$H_{ud} = \sum_{i=1}^N \tau_{12} (c_{i,u}^\dagger c_{i,d} + h.c.) + U_{12} n_{i,u} n_{i,d} \quad (\text{A.4})$$

In order to minimize scattering effects at the boundaries between the scattering region and the noninteracting leads, the interaction U is turned on adiabatically within the region of N_1 (see A.1).

$$U^{upper}(j) = U * \left(1 - \frac{1}{\exp(\beta * j - j') + 1}\right) \quad (\text{A.5})$$

$$U^{lower}(j) = U * \frac{1}{\exp(\beta * (j - N - N_1 + j') + 1)} \quad (\text{A.6})$$

The values of N_1 and β are chosen, such that all interactions are maximal and constant throughout the whole scattering region. Further the maximal value of the on-chain interaction equals the maximal value of the interchain interaction, i.e. $U_{max} = U_{12,max}$.

A.1.2. Model II

Since we observe strong boundary effects (see below) with model I, we also consider a second model with leads at each of the four ends, as illustrated Figure A.2. The Hamiltonian consists of the same three parts, extended by the extra leads.

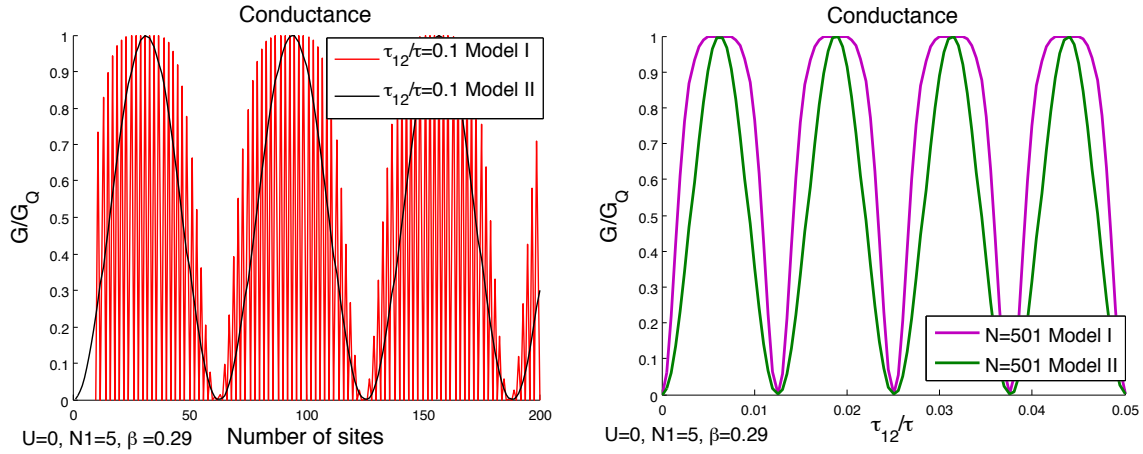
$$H = H_u + H_d + H_{ud} \quad (\text{A.7})$$

Hamiltonian of the upper/lower chain with $s = u, d$, respectively:

$$H_s = \sum_{i=-\infty}^{\infty} -\mu n_{i,s} + \tau (c_{i+1,s}^\dagger c_{i,s} + h.c.) + \sum_{i=-N_1+1}^{N+N_1} U n_{i,s} n_{i+1,s} \quad (\text{A.8})$$

Hopping and interactions are the same as in the first model:

$$H_{ud} = \sum_{i=1}^N \tau_{12} (c_{i,u}^\dagger c_{i,d} + h.c.) + U_{12} n_{i,u} n_{i,d} \quad (\text{A.9})$$



(a) Conductance plotted as a function of the length of the scattering region: The red curve belongs to model I, the black line depicts conductance of model II. The smaller oscillation is an effect of the finite ends of the chains in model I.

(b) Conductance plotted as a function of the interchain hopping: In model II the conductance oscillate sinusoidal, in model I the oscillation is broader.

Figure A.3.: Conductance as a function of number of sites and interchain hopping τ_{12} for model I and II. The comparison shows that the missing leads in Model I lead to extra boundary effects.

The interaction U is turned on adiabatically, such that within the scattering region the interaction is constant and maximal, as in the first model.

In both models the conductance is computed with the Landauer formula (4.37), with transmission in between the upper, left lead and the lower, right lead, i.e. in between the sites $(-N1, u)$ and $(N+N1, d)$:

$$G = \frac{e^2}{h} |2\pi\rho_{lead}(0)\tau^2\mathcal{G}_{-N1,u;N+N1,d}(0)|^2 \quad (\text{A.10})$$

If the temperature $T \neq 0$ and $U = 0$ the conductance in between the same site is computed with Landauer-Büttiker formula:

$$G = \frac{-e^2}{h} \int d\epsilon f'(\epsilon) |2\pi\rho_{lead}(\epsilon)\tau^2\mathcal{G}_{-N1,u;N+N1,d}(\epsilon)|^2 \quad (\text{A.11})$$

where f denotes the Fermi function.

A.2. Results

In the conductance of model I (Fig. A.3a) different oscillations can be observed. On the one hand, the conductance depends strongly on the length of the scattering region. If the number of sites of the central region N is even, a zero conductance is computed, if N is odd the conductance is finite. Further an envelope oscillations is observed. Its width B depends on the interchain hopping τ_{12} as $B \propto 1/\tau_{12}$.

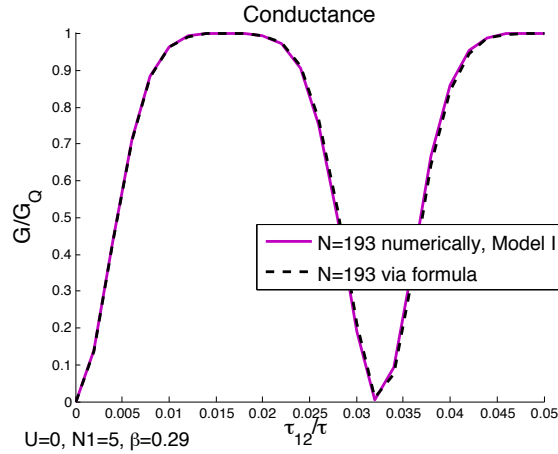


Figure A.4.: Comparison of numerical computed conductance with the transmission calculated with eq.(A.14) of model I. The transmission equation is in perfect agreement with the numerically computed conductance.

If the conductance is plotted as a function of the interchain hopping τ_{12} for different values of the length N (Fig. A.3b), again one observes an oscillating conductance with a width proportional to $1/N$.

Using the well known dispersion relation of the tight-binding-chain

$$\omega = -2\tau * \cos(k) \quad (\text{A.12})$$

the velocity of an electron propagating through one chain can be computed. The time t an electron needs to pass the scattering region is

$$t = N/v = N/\frac{d\omega}{dk} \quad (\text{A.13})$$

With an intrachain hopping of $\tau = 1$ and $k_F = \pi/2$ this leads to a velocity of $v = 2$. Interchain hopping τ_{12} is neglected in this calculation, but if τ_{12} is small, this is a good approximation. If one assumes that the electron propagates through the scattering region, while hopping back and forth and that it becomes reflected at the ends of the chain, where no leads are connected, then all possible ways of the particle can be added up, including the quantum mechanical phase. The probability that the particle has changed the chain after passing the whole scattering region of length N is proportional to $\sin(\tau_{12}t)$ and respectively that it did not change the chain proportional to $\cos(\tau_{12}T)$. Thus the system can be considered in an analogy to a Fabry-Perot-Interferometer. This leads to the following relation for the transmission:

$$T \approx \left| \sin\left(\frac{\tau_{12}N}{2\tau \sin k}\right) + \cos^2\left(\frac{\tau_{12}N}{2\tau \sin k}\right) e^{i(N+1)\pi} \sin\left(\frac{\tau_{12}N}{2\tau \sin k}\right) \frac{1}{1 - e^{iN\pi} \sin^2(\tau_{12}N/(2\tau \sin k))} \right|^2 \quad (\text{A.14})$$

This equation is in very good agreement with the numerical computed conductance for small τ_{12} , even if $\omega \neq 0$.

The conductance of model II plotted as a function of the scattering length N does not show the even-odd oscillations of the first model. The conductance has a sinusoidal dependence of

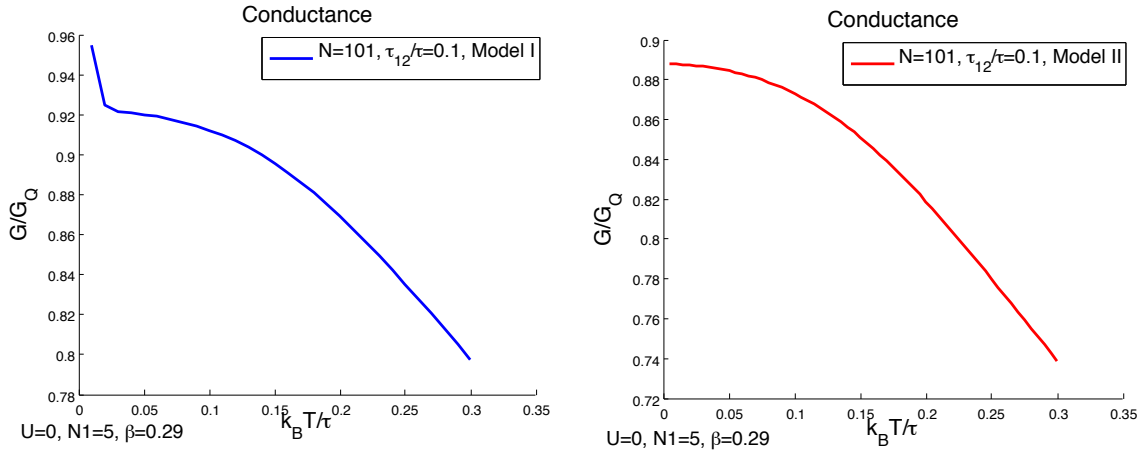
N and the interchain hopping τ_{12} (Fig. A.3). The transmission through this system can be regarded analogously to the transmission of the first model by adding up all possible ways to propagate from the upper, left lead to the lower, right lead. Due to the extra two leads, there is only one possible way. Thus the transmission can be described via

$$T \approx \sin^2(\tau_{12} * N / (2\tau \sin(k))) \quad (\text{A.15})$$

with k and T computed as described above. Again this relation is in very good agreement with the numerical computed results for small τ_{12} .

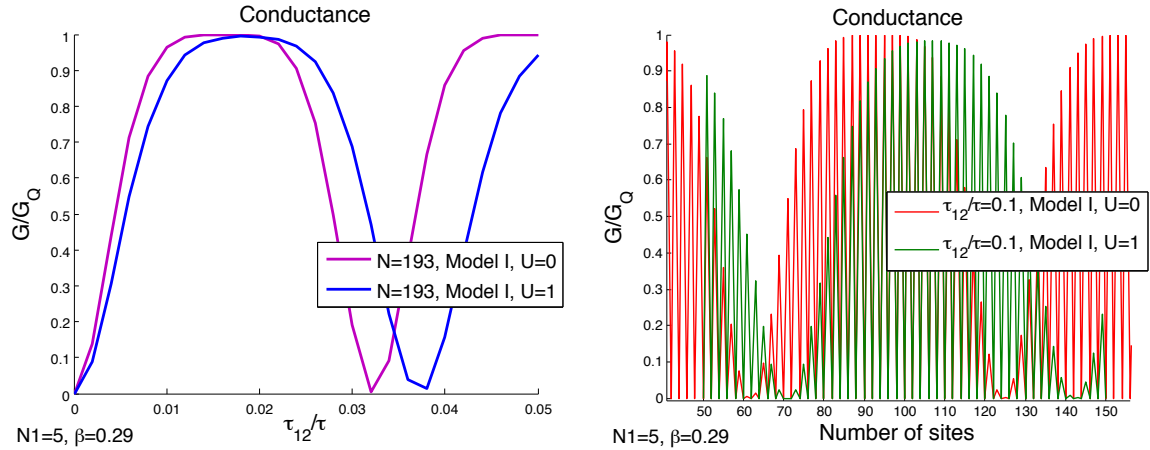
The conductance as a function of the temperature decreases with increasing temperature (Fig. A.5), because the velocity of the electron decreases with rising temperature. Interchain hopping and the site number N are chosen such that for $T = 0$ the conductance is nearly at its maximum. The smaller velocity leads to oscillations with changed oscillation length and thus the conductance decreases, because the oscillation is changed with respect to number of sites and τ_{12} . In model I the decrease is even stronger with low temperatures (Fig. A.5a). This can be explained considering that there are two oscillations in the conductance, one due to the velocity one because of the quantum mechanical phase. With small temperatures the second one is the leading one.

If now model I is considered with interactions (Fig. A.6a and A.6b), it is noticed that the width of the oscillations is changed, but not the appearance. The interaction changes the effective value of τ_{12} and the effective value of the velocity of the electron through the scattering region. The maximum of the conductance becomes slightly smaller. In the noninteracting case $G_{max} = 1$, in the interacting case it lies below this value depending on the choice of τ_{12} and N . The impact of interactions on model II is the same, the effective hopping amplitude and the velocity become smaller and thus the width of the oscillation is changed.



- (a) Conductance plotted as a function of temperature for model I. With increasing temperature the velocity of the electrons decreases, which leads to decreasing conductance, because the oscillation length is changed and thus the position within the oscillation. This effect is even enhanced for small temperature, because in this regime the smaller quantum mechanically oscillations are more important.
- (b) Conductance plotted as a function of temperature for model II. With increasing temperature the velocity of the electrons decreases, which leads to decreasing conductance, because the oscillation length is changed and thus the position within the oscillation.

Figure A.5.: Conductance plotted as a function of temperature for both models.



- (a) Conductance plotted as a function of the inter-chain hopping τ_{12} of model I.
- (b) Conductance plotted as a function of the length of the scattering region N of model I.

Figure A.6.: Comparison of the interacting with the noninteracting system. Interaction does not change the physics within the system, but renormalizes the effective value of the inter-chain hopping τ_{12} and the effective velocity, which can be read off the changed oscillation length.

Bibliography

- [1] B. J. van Wees, H. van Houten, C. W. J. Beenakker, J. G. Williamson, L. P. Kouwenhoven, D. van der Marel, and C. T. Foxon. Quantized conductance of point contacts in a two-dimensional electron gas. *Physical Review Letters*, 60(9):848–850, 02 1988.
- [2] D A Wharam, T J Thornton, R Newbury, M Pepper, H Ahmed, J E F Frost, D G Hasko, D C Peacock, D A Ritchie, and G A C Jones. One-dimensional transport and the quantisation of the ballistic resistance. *Journal of Physics C: Solid State Physics*, 21(8):L209, 1988.
- [3] K. J. Thomas, J. T. Nicholls, M. Y. Simmons, M. Pepper, D. R. Mace, and D. A. Ritchie. Possible spin polarization in a one-dimensional electron gas. *Physical Review Letters*, 77(1):135–138, 07 1996.
- [4] F. Bauer, J. Heyder, E. Schubert, D. Borowsky, D. Taubert, B. Bruognolo, D. Schuh, W. Wegscheider, J. von Delft, and S. Ludwig. Microscopic origin of the 0.7-anomaly in quantum point contacts. *submitted to Nature*.
- [5] S. Andergassen, T. Enss, V. Meden, W. Metzner, U. Schollwöck, and K. Schönhammer. Renormalization-group analysis of the one-dimensional extended hubbard model with a single impurity. *Physical Review B*, 73(4):045125–, 01 2006.
- [6] C. Karrasch, T. Enss, and V. Meden. Functional renormalization group approach to transport through correlated quantum dots. *Physical Review B*, 73(23):235337–, 06 2006.
- [7] Walter Metzner, Manfred Salmhofer, Carsten Honerkamp, Volker Meden, and Kurt Schönhammer. Functional renormalization group approach to correlated fermion systems. *Reviews of Modern Physics*, 84(1):299–352, 03 2012.
- [8] E.Schubert D.Borowsky D.Taubert B.Bruognolo D.Schuh W.Wegscheider J.von Delft S.Ludwig F.Bauer, J.Heyder. 0.7 anomaly of quantum point contacts treatment of interaction with functional renormalization group. Master’s thesis, LMU München, 2008.
- [9] Christoph Karrasch. Transport through correlated quantum dots - a functional renormalization group approach. Master’s thesis, 2006.
- [10] V.Meden. Funktionale renormierungsgruppe.
- [11] S. Jakobs. Renormierungsgruppen-methoden fuer nichtlinearen transport. Master’s thesis, 2003.
- [12] Severin Jakobs. *Functional renormalization group studies of quantum transport through mesoscopic systems*. PhD thesis, RWTH Aachen, 2009.

-
- [13] T.Enss. *Renormalization, Conservation Laws and Transport in Correlated Electron Systems*. PhD thesis, 2005.
- [14] TIM R. MORRIS. The exact renormalization group and approximate solutions. *International Journal of Modern Physics A*, 09(14):2411–2449, 2013/03/07 1994.
- [15] T.Heinzel. *Mesoscopic Electronics in Solid State Nanostructures*. WILEY-VCH, 2007.
- [16] Y. Blanter Y. Nazarov. *Quantum Transport - Introduction to Nanoscience*. Cambridge University Press, 2009.
- [17] M. Büttiker. Quantized transmission of a saddle-point constriction. *Physical Review B*, 41(11):7906–7909, 04 1990.
- [18] A P Micolich. What lurks below the last plateau: experimental studies of the $0.7 \frac{2e^2}{h}$ conductance anomaly in one-dimensional systems. *Journal of Physics: Condensed Matter*, 23(44):443201, 2011.
- [19] E. J. Koop, A. I. Lerescu, J. Liu, B. J. Wees, D. Reuter, A. D. Wieck, and C. H. Wal. The influence of device geometry on many-body effects in quantum point contacts: Signatures of the 0.7 anomaly, exchange and kondo. 20(6):433–441, 2007.
- [20] K.Flensberg H.Bruus. *Many-Body Quantum Theory in Condensed Matter Physics*. Oxford Graduate Texts, 2004.
- [21] N.Ufer. Conductance anomalies in quantum point contacts functional renormalization group applied to a 2d hubbard model. Master’s thesis, 2011.
- [22] Alexander Altland, Yuval Gefen, and Bernd Rosenow. Incoherent scatterer in a luttinger liquid: A new paradigmatic limit. *Physical Review Letters*, 108(13):136401–, 03 2012.
- [23] S. Nakaharai, J. R. Williams, and C. M. Marcus. Gate-defined graphene quantum point contact in the quantum hall regime. *Physical Review Letters*, 107(3):036602–, 07 2011.

Acknowledgements

First of all, I would like to thank Jan von Delft for giving me the opportunity to write my thesis in his group. I learnt a lot during this year and had a very good time working in this group.

A very special thanks goes to Florian Bauer und Jan Heyder, which I always could ask so much questions and from whom I learnt a lot. They have been very patient supervisors, brilliant explainers and show real enthusiasm for physics. They introduced me to the world of vertex functions, quantum point contacts and -which might has been the hardest- C++ and clusters. Moreover, they let me use their ODE-solver as well as their matrix class.

Further Thanks goes to

... the whole group, I won't list all the names, which all helped with advice, coffee breaks and "Klönschnacks". Thank you for this kind working atmosphere where no one hesitates to help.

... Kathi for sharing so much chocolate with me and teaching me Boarisch.

...Michi for a lot of (computer) advice and stupid jokes.

...Stefan, Friederike, Jonas for calming me down and cake.

...My whole family (my parents, Marie-Lena, Philipp, my grandmothers and Meret) for everything and support in any imaginable way. Encouraging words, postcards, tea...

Hiermit erkläre ich, die vorliegende Arbeit selbständig verfasst zu haben und keine anderen als die in der Arbeit angegebenen Quellen und Hilfsmittel benutzt zu haben.

München, den 2. 4. 2013